GL-TR-89-0335

AD-A219 802

NORSAR Basic Seismological Research
1 January - 30 September 1989

Editor:
Svein Mykkeltveit

NTNF/NORSAR
Post Box 51
N-2007 Kjeller, Norway

29 November 1989

Scientific Report No. 3

APPROVED FOR PUBLIC RELEASE; DISTRIBUTION UNLIMITED

GEOPHYSICS LABORATORY
AIR FORCE SYSTEMS COMMAND
UNITED STATES AIR FORCE
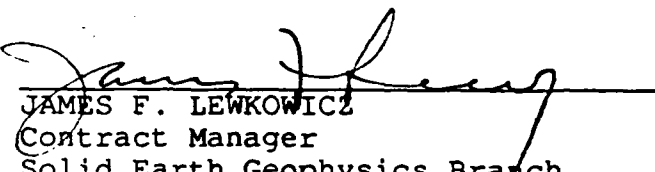HANSCOM AIR FORCE BASE, MASSACHUSETTS 01731-5000

90 03 28 122

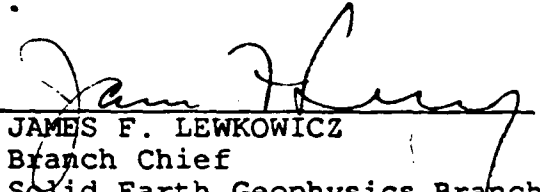This technical report has been reviewed and is approved for publication.

JAMES F. LEWKOWICZ
Contract Manager
Solid Earth Geophysics Branch
Earth Sciences Division

JAMES F. LEWKOWICZ
Branch Chief
Solid Earth Geophysics Branch
Earth Sciences Division

FOR THE COMMANDER

DONALD H. ECKHARDT, Director
Earth Sciences Division

REPORT DOCUMENTATION PAGE

Form Approved
OMB No 0704-0188

1a. REPORT SECURITY CLASSIFICATION	1b RESTRICTIVE MARKINGS
Unclassified	

2a. SECURITY CLASSIFICATION AUTHORITY	3 DISTRIBUTION/AVAILABILITY OF REPORT
	Approved for public release;
2b. DECLASSIFICATION/DOWNGRADING SCHEDULE	Distribution unlimited

4 PERFORMING ORGANIZATION REPORT NUMBER(S)	5 MONITORING ORGANIZATION REPORT NUMBER(S)
	GL-TR-89-0335

6a. NAME OF PERFORMING ORGANIZATION	6b OFFICE SYMBOL (If applicable)	7a NAME OF MONITORING ORGANIZATION
NTNF/NORSAR		Geophysics Laboratory

6c. ADDRESS (City, State, and ZIP Code)	7b ADDRESS (City, State, and ZIP Code)
Post Box 51	Hanscom Air Force Base
N-2007 Kjeller, Norway	Massachusetts 01731-5000

8a. NAME OF FUNDING/SPONSORING ORGANIZATION	8b OFFICE SYMBOL (If applicable)	9 PROCUREMENT INSTRUMENT IDENTIFICATION NUMBER
Defence Advanced Research Projects Agency	NMRO	Contract No. F49620-89-C-0038

8c. ADDRESS (City, State, and ZIP Code)	10 SOURCE OF FUNDING NUMBERS			
	PROGRAM ELEMENT NO.	PROJECT NO.	TASK NO	WORK UNIT ACCESSION NO.
1400 Wilson Blvd.				
Arlington, VA 22209-2308	62714E	9A10	DA	BH

11. TITLE (Include Security Classification)

NORSAR Basic Seismological Research - 1 January - 30 September 1989

12 PERSONAL AUTHOR(S)

Svein Mykkeltveit (ed.)

13a. TYPE OF REPORT	13b. TIME COVERED	14. DATE OF REPORT (Year, Month, Day)	15. PAGE COUNT
SCIENTIFIC REP. 3	FROM 89/01/01 TO 89/09/30	1989 November 29	78

16 SUPPLEMENTARY NOTATION

17.	COSATI CODES		18. SUBJECT TERMS (Continue on reverse if necessary and identify by block number)
FIELD	GROUP	SUB-GROUP	Surface wave modelling; source and structure inver-
			sions; topographic effects; local magnitudes; regional
			attenuation, network detection; phase association;

19. ABSTRACT (Continue on reverse if necessary and identify by block number)   region-specific knowledge.

This Annual Technical Report describes the work accomplished under Contract No. F49620-C-89-0038 during the period 1 January - 30 September 1989. The report comprises five separate investigations, addressing the main topics within the scope of work.

As part of our effort to enhance the performance of the Intelligent Monitoring System, we have embarked on a series of projects to aid in the understanding of the behavior of the tectonic processes currently acting within Norway as well as wave propagation effects for observed

20 DISTRIBUTION/AVAILABILITY OF ABSTRACT	21 ABSTRACT SECURITY CLASSIFICATION
☐ UNCLASSIFIED/UNLIMITED ☐ SAME AS RPT ☐ DTIC USERS	UNCLASSIFIED

22a NAME OF RESPONSIBLE INDIVIDUAL	22b TELEPHONE (Include Area Code)	22c OFFICE SYMBOL
James Lewkowicz	(617) 377-3028	GL/LWH

DD Form 1473, JUN 86   Previous editions are obsolete   SECURITY CLASSIFICATION OF THIS PAGE

19. (cont.)

seismic phases. In paragraph 2.1 of this report, new information is conveyed about earthquake faulting mechanisms and quantification of the structural information contained within waveform data observed in Norway.

An analysis of the location capabilities of NORESS and ARCESS, and of the 3-component stations within the arrays, leads to the following conclusions concerning 3-component slowness solutions for P waves: (1) There is a relatively large scatter in the solutions for events from the same source region, and (2) there are significant differences between the solutions at the different stations. In the contribution of paragraph 2.2 of this report, topographic effects have been analyzed by comparing slowness solutions for P from explosions in three different source regions. Numerical modelling demonstrates that surface topography can explain about half of the slowness anomalies observed on three-component stations.

Paragraph 2.3 is a status report on work related to local magnitudes and regional wave attenuation. The work comprises the establishment of a large data base of regional records, the development of analysis tools and strategies, and subsequent data analysis aimed at derivation of regional wave attenuation relationships and the development of a new magnitude scale for Norway and adjacent areas.

The paper of paragraph 2.4 presents a method for associating phase detections from a network of stations, which is analogous to the conventional delay-and-sum beamforming commonly applied in array detection processing. Examples of application of this method are given, based on data recorded at the three regional arrays (NORESS, ARCESS, FINESA) in Fennoscandia. The problem of continuously monitoring the regional seismic noise field is also addressed, with the purpose of obtaining a quantitative assessment of the upper limit of magnitudes of seismic events that would go undetected by a given network.

Two investigations aimed at deriving region-specific knowledge from analysis of NORESS data are described in paragraph 2.5. The first investigation is based on a study of the complete NORESS detection lists for the period 1985-1988, and statistics on phase velocities and arrival azimuth residuals are obtained for events reported in the regional network bulletins. The second investigation is a detailed study of 103 events in the western Norway area. The study shows that arrival azimuth residuals observed at NORESS for Pn and Sn phases vary systematically with source region in the western Norway area.

Preface

Under Contract No. F49620-C-89-0038, NTNF/NORSAR is conducting research within a wide range of subjects relevant to seismic monitoring. The emphasis of the research program is on developing and assessing methods for processing of data recorded by networks of small-aperture arrays and 3-component stations, for events both at regional and teleseismic distances. In addition, more general seismological research topics are addressed.

Each quarterly technical report under this contract presents one or several separate investigations addressing specific problems within the scope of the statement of work. Summaries of the research efforts within the program as a whole are given in annual technical reports.

This Scientific Report No. 3 is the annual technical report for the period 1 January - 30 September 1989. It contains five separate contributions, addressing the main topics within the scope of work for this contract.

NORSAR Contribution No. 413

iii

Table of Contents

1 SUMMARY

This Annual Technical Report describes the work accomplished under Contract No. F49620-C-89-0038 during the period 1 January - 30 September 1989. The report comprises five separate investigations, addressing the main topics within the scope of work.

As part of our effort to enhance the performance of the Intelligent Monitoring System, we have embarked on a series of projects to aid in the understanding of the behavior of the tectonic processes currently acting within Norway as well as wave propagation effects for observed seismic phases. In paragraph 2.1 of this report, new information is conveyed about earthquake faulting mechanisms and quantification of the structural information contained within waveform data observed in Norway.

An analysis of the location capabilities of NORESS and ARCESS, and of the 3-component stations within the arrays, leads to the following conclusions concerning 3-component slowness solutions for P waves: (1) There is a relatively large scatter in the solutions for events from the same source region, and (2) there are significant differences between the solutions at the different stations. In the contribution of paragraph 2.2 of this report, topographic effects have been analyzed by comparing slowness solutions for P from explosions in three different source regions. Numerical modelling demonstrates that surface topography can explain about half of the slowness anomalies observed on three-component stations.

Paragraph 2.3 is a status report on work related to local magnitudes and regional wave attenuation. The work comprises the establishment of a large data base of regional records, the development of analysis tools and strategies, and subsequent data analysis aimed at derivation of regional wave attenuation relationships and the development of a new magnitude scale for Norway and adjacent areas.

The paper of paragraph 2.4 presents a method for associating phase detections from a network of stations, which is analogous to the conventional delay-and-sum beamforming commonly applied in array detection processing. Examples of application of this method are given, based on data recorded at the three regional arrays (NORESS, ARCESS, FINESA) in Fennoscandia. The problem of continuously monitoring the regional seismic noise field is also addressed, with the purpose of obtaining a quantitative assessment of the upper limit of magnitudes of seismic events that would go undetected by a given network.

Two investigations aimed at deriving region-specific knowledge from analysis of NORESS data are described in paragraph 2.5. The first investigation is based on a study of the complete NORESS detection lists for the period 1985-1988, and

statistics on phase velocities and arrival azimuth residuals are obtained for events reported in the regional network bulletins. The second investigation is a detailed study of 103 events in the western Norway area. The study shows that arrival azimuth residuals observed at NORESS for Pn and Sn phases vary systematically with source region in the western Norway area.

2 SUMMARY OF TECHNICAL FINDINGS AND ACCOMPLISHMENTS

2.1 Surface Wave Modelling for Source and Structure Inversions

Introduction

As a part of our effort to enhance the performance of the Intelligent Monitoring System we have embarked on a series of projects to aid in the understanding of the behavior of the tectonic processes currently acting within Norway as well as wave propagation effects for observed seismic phases. A proper understanding of dynamic processes within the crust and upper mantle requires a detailed knowledge about the occurrence of earthquakes and the medium through which the seismic waves propagate.

Norway and its surrounding areas, in particular the northern continental margin, have until recently been relatively poorly covered in terms of seismic instrumentation. In the last decade the situation has been much improved, however, through the installation of new regional and local networks and arrays. This increased number of stations has resulted in more detailed delineation of seismicity patterns as well as improved focal mechanism solutions and local magnitude scales. The methods of matching synthetic waveforms to observed data for the retrieval of source processes has further increased our ability to discriminate various source types from the fundamental observations of seismic data. This methodolgy is strongly coupled to the determination of crustal structure for which we have also gained much information.

The purpose of this contribution is to convey significant new information about earthquake faulting mechanisms and quantification of the structural information contained within waveform data observed within Norway and along the Norwegian continental margin areas. Discussion of the results of the modelling of specific events is left to a further report, or can be found in Bungum *et. al.* (1989).

Source Mechanism Determination

For an area such as the Norwegian continental shelf, with low-to-intermediate seismicity as described above, the earlier (pre 1980) limitations in instrumental coverage also severely limited the possibilities for obtaining information about crustal stress conditions through earthquake focal mechanisms. More and better seismological stations as well as improved methods for source analysis through waveform modelling have now changed this situation markedly.

A major effort towards obtaining new focal mechanism solutions has resulted in 28 new solutions. Focal mechanism solutions for several of the earthquakes

3

proved to be quite difficult to obtain using the conventional first motion analysis. There either were not enough data to well constrain the nodal planes or errors were introduced in the take-off angles from the source due to misinterpretation of the travel path of the seismic phase because of the complicated geometry of the crust-mantle interface (as was the case for the event in Figure 2.1.1, Event 5 in Table 2.1.1). In six of these cases, source mechanisms have been retrieved through waveform modelling, using the same method as Hansen *et. al.* (1989) applied for two of the largest earthquakes in the area (Events 2 and 5 in Table 2.1.1). The results have been found to be very stable even when data from only one station have been used (NORSAR long-period for Event 1, NORESS intermediate-period for Events 3 and 4).

Since several events were found to have produced fairly simple and well recorded long period surface waves, an approach of source mechanism retrieval was adopted that combines broad-band waveform modelling with the more conventional first motion analysis. The method (Hansen, 1989) consists of low pass filtering the broad-band records from the NORESS array (NRS) and Kongsberg (KONO) to emphasize the low frequency waves up to about 6 seconds period and then matching the waveforms to synthetic seismograms computed for a given earth structure and source mechanism in both a forward and inverse sense. Green's functions were computed using the Locked Mode Approximation method of Harvey (1981) for a crust-mantle structure derived from Mykkeltveit (1980) for the crust and Stuart (1978) for the upper mantle.

The results of this modelling are illustrated in Figures 2.1.1 (forward modelling) and 2.1.2 (inverse modelling) for Events 5 and 2, respectively. Three-component seismograms recorded for each event are shown after filtering and rotation to vertical, radial, and transverse components. The corresponding synthetic seismograms are shown just below the observed ones. The method was first applied to Event 5 (Figure 2.1.1) where excellent results were obtained. The inverse procedures were then developed and the data set for the event in Figure 2.1.2 was augmented to include the three-component Kongsberg (KONO) long period data. To the right of Figures 2.1.1 and 2.1.2 are the focal mechanism drawings (lower hemisphere stereographic projections) for the nodal planes obtained from the waveform modelling together with the first motion data. It is obvious that the first motion data are to some extent discordant, either due to incorrect readings or false interpretations. Experimenting with different velocity models for location, and varying the source depth failed to improve the interpretation of the first motion data. However, they were useful in helping to discriminate between say two different waveform solutions and serve to supply constraints on further interpretation of velocity models in the area. Several of these events were verified with forward waveform modelling even if the inversion procedure was not deemed warranted by the data. As an example, Figures 2.1.3 and 2.1.4 illustrate the fit from forward modelling of two earthquakes (Events 4

and 1 in Table 2.1.1) near the Lofoten Islands at a distance of more than 800 kilometers from the recording stations at NORESS (Figure 2.1.3) and NORSAR (Figure 2.1.4). It is very encouraging to find that initial interpretations of the sparse amount of first motion data can be verified to a much higher degree of confidence.

Due to the complexity of the crust and upper mantle structure in the vicinity of the earthquakes, it was necessary to explore the effect of the assumed velocity structure on the low frequency waveform modelling. Since we are observing phases with wavelengths on the order of 20 kilometers and longer, much of the complexity affecting the high frequency first motion data is smoothed out. The structures used for computing synthetic seismograms therefore reflected the average, and more homogeneous, properties sampled along the majority of the travel path from the earthquake to the receiving stations. By observing the change in the synthetic waveforms as a function of structural model and earthquake source depth it was verified that the solutions for the focal mechanisms and source depths are quite robust for the long period data. Variations in the compression and tension axes of the focal sphere were found to be less than about 5 degrees due to changes in velocity models for a single station solution, and were improved with the inclusion of a second three-component station (KONO). It was also found that source depths could be verified from the modelling to a precision of about ± 5 km.

For Event 2 (Fig. 2.1.2), the waveform fit is excellent. It is seen from the focal mechanism plot that the fault plane solution would be difficult to obtain from first motion data alone. In fact, an earlier interpretation of the first motion data of this event indicated a normal fault with a near vertical axis of maximum compression. However, the waveform modelling shown here for this event completely rules out this type of solution. Instead, the solution for this earthquake clearly indicates oblique thrust faulting in response to a regional stress field exhibiting NW-SE horizontal compression.

For most of the 28 new events, a similar amplitude modelling has not been feasible because of the very different character of the long period waveforms. Small events did not have enough energy in the long periods for them to be observed above the noise levels, while some larger events produced far too complex waveforms to be easily interpreted. The complex seismograms are likely a result of the rapidly changing crustal structure between events out to sea and the seismometers located in southeastern Norway. In these cases, a solution using first motions only is given, where a combination of local and teleseismic data helps in constraining the nodal planes. However, when the events are within local distance ranges, the higher order surface wave trains can be summed to produce body-waves that can be fit to the observations up to 2 or 3 Hertz. Figure 2.1.5 shows an example of such an event (Event 6) occurring very near the NORESS and NORSAR arrays with recording stations ranging from about 15 to 85 kilome-

ters. Figure 2.1.5 shows that the velocity model is only crucial to events at large distances at higher frequencies. An approach to improve this result is outlined in the next section as an improvement to the velocity models.

Improved Velocity Models

Although we have achieved good results in inverting for source parameters by matching synthetic an ' real seismograms, our success has been limited since we have only been able to do this for a small number of events and at low freq encies. Since we are using a laterally homogeneous modelling technique, it can be argued that such a technique may never be suitable for inversion in situations where the structure depth dependence changes significantly along the source-receiver propagation path, such as earthquakes in the oceanic crust that are recorded within the continental crust. Unfortunately the problem of regional forward wave propagation modelling through arbitrary inhomogeneous media is effectively intractable at intermediate and high frequencies, and even at low frequencies it can only be accomplished by making assumptions on the nature of the media inhomogeneities, such as slow and weak lateral variations, that are often violated in real world situations.

The success that we have had demonstrates that, at least in certain situations, laterally homogeneous modelling can be used to "image out" both the structure and the source parameters. These situations seem to involve cases where the source-receiver propagation paths stay within the boundaries of the continental crust, which lends more credence to the laterally homogeneous assumption. There are not many crustal events, however, that are large enough to produce significant energy in the low frequencies. We would like to be able to investigate small crustal events, such as local and near-regional explosions, but we can only do this by looking at higher frequencies where the source produces significant energy. When we look at the events that we can match well at low frequencies, our matches deteriorate rapidly as we increase the frequency bandwidth. which is not surprising considering the relatively crude nature of the structural models that we have been using. As we raise the frequency content of our synthetic seismograms, we find that they become increasingly sensitive to detailed changes in the structural model. Thus it becomes evident that, in order to match synthetic and real data at higher frequencies, it will be necessary to invert for structural parameters as well as for source parameters.

We have begun a systematic approach to the comparison-inversion problem which will take advantage of some recent work that has been done in this area and which should provide a clear and realizable path to detailed structural models that will produce optimal fits between the real and synthetic seismograms. The core of our method involves a modified version of the direct inversion technique developed by Gomberg and Masters (1988) which uses iterative linear inversion based upon differential seismograms that are analytically computed from

6

a Locked Mode representation of the solution. We will carry out this inversion in stages, starting with very low frequency, band limited comparisons of real and synthetic seismograms which will determine the gross characteristics of the structure. We will then proceed to open up the bandwidth of comparison in steps and invert for increasingly detailed aspects of the structural model while maintaining the average characteristics that were determined in the lower band inversions for both source and structure. At the same time it may be necessary as we go up in frequency to re-estimate the source parameters for each more complex structure iteration. In this manner we hope to obtain the best average velocity-depth dependencies in specific tectonic provinces.

We have implemented the core computations for the differential seismograms at NORSAR and CIRES based on the Locked Mode methods of Harvey (1981). At this stage we are able to compute perturbation seismograms that can be used to determine the effect on the seismogram of small changes in layer velocities. The current implementation is functionally identical to that of Gomberg and Masters in that it is a perturbation implementation which assumes that only the eigenvalues change, as opposed to a true differential implementation which accounts for both changes in the eigenfunctions and eigenvalues. The perturbation seismograms become inaccurate as the source-receiver distance decreases and the frequency increases, so we are in the process of implementing the exact differential seismogram computations and undertaking a detailed study to show where the perturbation approximation breaks down. We have implemented the core differential computations in a significantly different manner from that of Gomberg and Masters which allows us to do the exact differential computations in a straightforward manner.

Roger A. Hansen
Danny J. Harvey, CIRES, University of Colorado

References

Bungum H., A. Alsaker, L.B. Kvamme and R.A. Hansen (1989): Seismicity and seismot·ctonics of Norway and nearby continental shelf areas. Submitted to *Journ. of Geophys. Research*

Gomberg, J. and T. Masters (1988): Waveform modelling using locked-mode synthetic and differential seismograms: application to determination of the structure of Mexico *Geophys. J.R. astr. Soc.*, 94, 193-218.

Hansen, R.A. (1989): Surface wave modelling and source parameter inversions of Norwegian earthquakes recorded at local and regional distances, *EOS Trans. AGU*, in press.

Hansen, R.A., H. Bungum and A. Alsaker (1989): Three recent larger earthquakes offshore Norway, *Terra Nova*, 1, 284-295.

Harvey, D. (1981): Seismogram synthesis using normal mode superposition: the locked mode approximation, *Geophys. J.R. astr. Soc.*, 66, 37-61.

Mykkeltveit, S. (1980): A seismic profile in southern Norway, *Pageoph.*, 118. 1310-1325.

Stuart, G.W. (1978): The upper mantle structure of the North Sea region from Rayleigh wave dispersion, *Geophys. J.R. astr. Soc.*, 52, 367-382.

No.	Reg.	Date	Lat N	Lon E	Depth	Mag.	T-axis Az	Dip	P-axis Az	Dip	Type
1	NN	810903	69.62	13.68	12C	4.7	49	38	301	22	RO
2	WN	860205	62.71	4.69	20C	4.9	198	55	303	10	R
3	WN	861026	61.83	3.20	14B	4.5	305	78	112	12	R
4	NN	880131	68.03	9.58	20C	4.3	92	24	329	51	NO
5	WN	890123	61.97	4.42	26A	5.1	239	72	124	8	R
6	SN	890410	60.61	11.40	22B	1.9	35	42	303	3	RO

Table 2.1.1. Earthquake focal mechanisms collected for this study, with the different columns indicating event number, region (SN, Southeastern Norway, WN, Western Norway, NN, Northern Norway), date (year, month, day), latitude, longitude, focal depth (A, precision ≤ 3 km; B, 4-6 km; C, 7-9 km, D, ≥ 10 km), magnitude (M_L), T-axis (minimum compression) azimuth and dip, P-axis (maximum compression) azimuth and dip, type of mechanism (N, normal; NO, normal oblique; R, reverse or thrust; RO, reverse oblique).
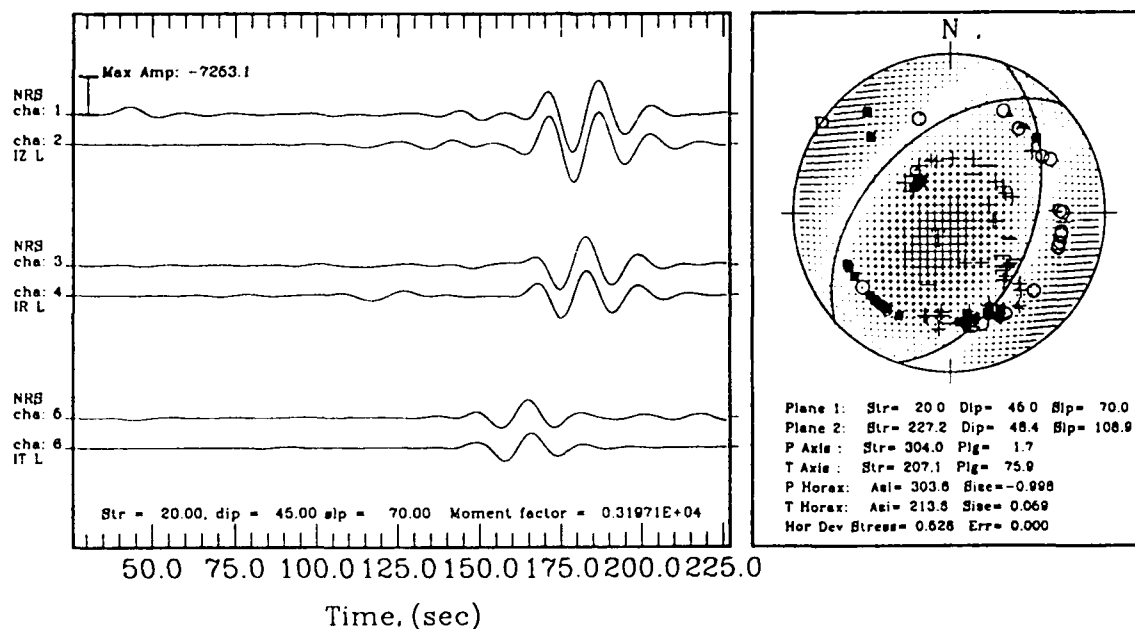
Figure 2.1.1. Focal mechanism solution from forward waveform modelling, Event 5, 23 January 1989. The *left* frame shows three components (vertical, radial and transverse) of NORESS broad band data together with theoretical seismograms from the double couple moment tensor immediately below each trace, while the *right* frame shows the double couple solution from the moment tensor. The first motion data not read by the authors are indicated by plus and minus signs for compressions and dilations, respectively.

Date: 02 05 86   1753

Figure 2.1.2. Focal mechanism solution from inversion of waveform data, Event 2, 5 February 1986. The *left* frame shows three components (vertical, radial and transverse) of NORESS broad band data and Kongsberg Long Period data together with theoretical seismograms from the deviatoric moment tensor immediately below each trace, while the *right* frame shows the best double couple solution from the moment tensor. The percent non-double couple for this event at these low frequencies is less than 1.

11

Date: 01 31 88   1853

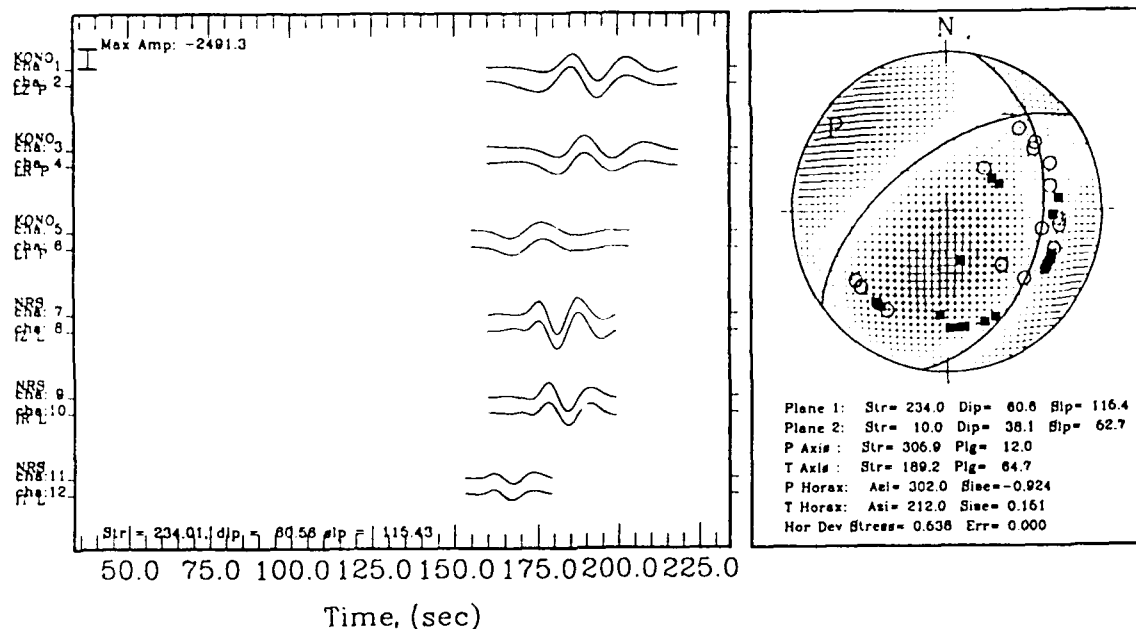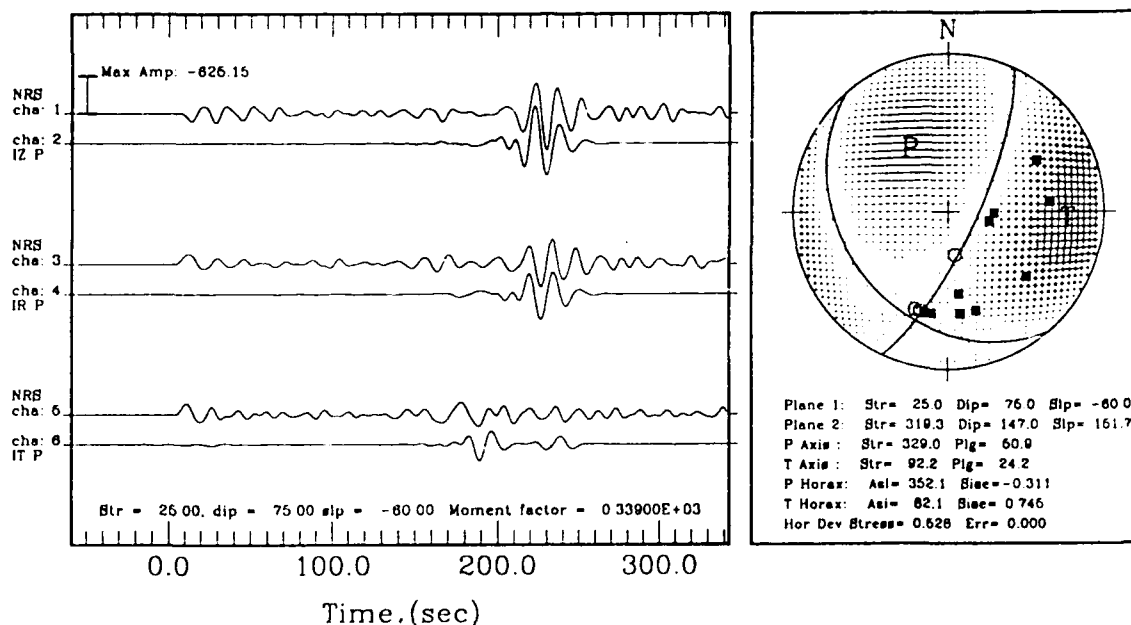Filtering   0 0.00   4 0.07
Green Function source depth = 20.0
nlvz1hz20jan31.grn   9/22/8917:34:24 NORSAR

Figure 2.1.3. Focal mechanism solution from forward waveform modelling for a Lofoten event of 31 January 1988. This figure illustrates the application of the modelling technique as applied to the NORESS Broad-Band recording of an event in Northern Norway at a distance of more than 800 km in the magnitude range of 4.0 to 4.5. The *left* frame shows three components (vertical, radial and transverse) of NORESS filtered Broad-Band data together with theoretical seismograms immediately below each trace, while the *right* frame shows the focal mechanism solution used in the waveform modelling.

Date: 09 03 81   1839

Max Amp: 494.72

NAO1
cha: 1

cha: 2
LZ P

NAO1
cha: 3

cha: 4
LR P

NAO1
cha: 6

cha: 6
LT P

Str = 178.00, dip = 80.00 slp =   45.00 Moment factor = 0.95407E+03

N

P

Plane 1:   Str= 178.0 Dip= 80.0 Slp= 45.0
Plane 2:   Str= 78.1 Dip= 46.9 Slp= 166.0
P Axis :   Str= 300.6 Plg= 21.7
T Axis :   Str= 48.6 Plg= 38.0
P Horax: Asi= 306.1 Sise=-0.826
T Horax: Asi= 38.1 Sise= 0.666
Hor Dev Stress= 0.707 Err= 0.000

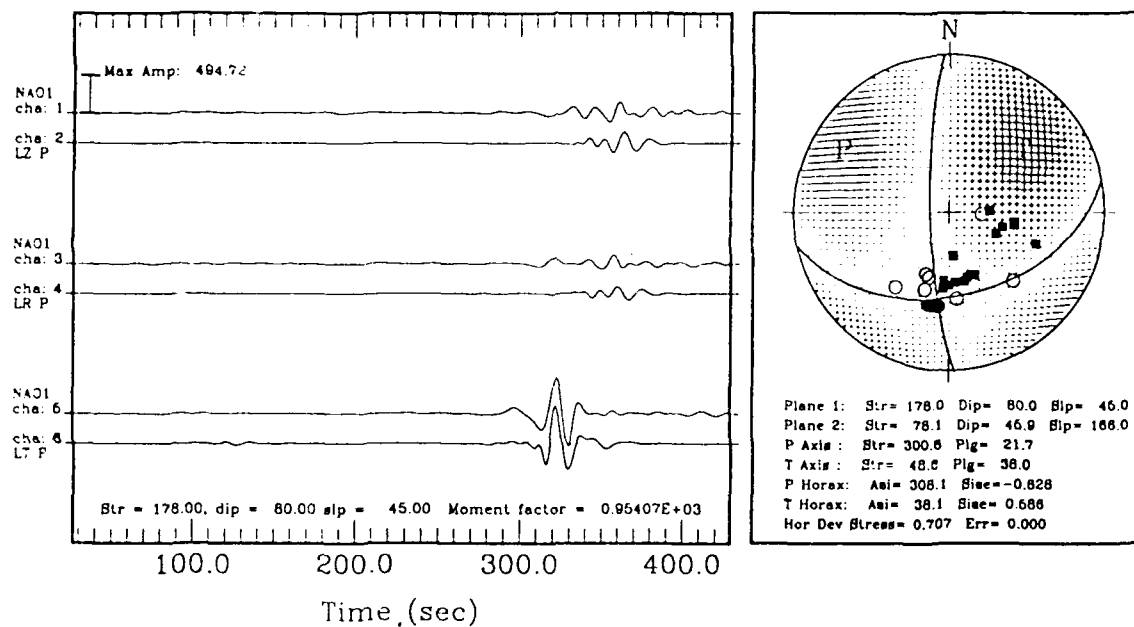100.0   200.0   300.0   400.0

Time (sec)

Filtering   0 0.00   4 0.10
Green Function source depth = 10.0
nlvz1hz10sep3.grn

10/17/8911:34:40 NORSAR

Figure 2.1.4. Focal mechanism solution from forward waveform modelling for a Lofoten event of 3 September 1981. This figure illustrates the application of the modelling technique as applied to the NORSAR LP recording of an event in Northern Norway at a distance of more than 800 km in the magnitude range of 4.5 to 5. The *left* frame shows three components (vertical, radial and transverse) of NORSAR Long Period data together with theoretical seismograms immediately below each trace, while the *right* frame shows the focal mechanism solution used in the waveform modelling. This figure illustrates the dominance of the Love wave component for solutions derived from waveform modelling.
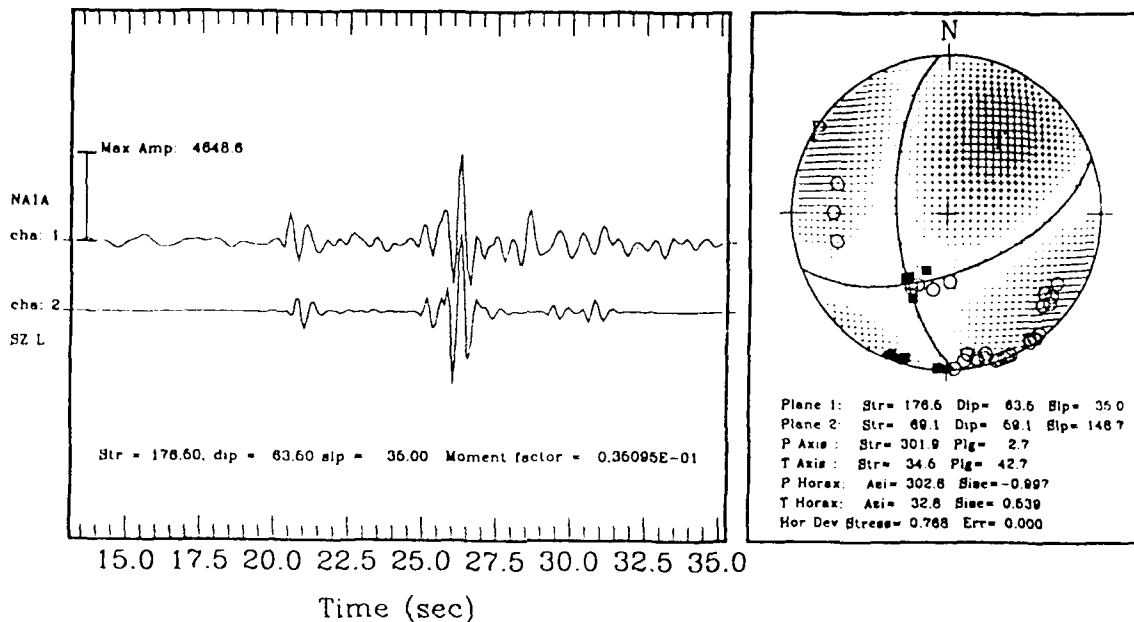
13

Date: 04 10 89 2114

Max Amp: 4648.6

NA1A

cha: 1

cha: 2

SZ L

Str = 176.60, dip = 63.60 slp = 36.00 Moment factor = 0.36095E-01

15.0 17.5 20.0 22.5 25.0 27.5 30.0 32.5 35.0

Time (sec)

N

Plane 1: Str= 176.6 Dip= 63.6 Slp= 35.0
Plane 2: Str= 69.1 Dip= 69.1 Slp= 146.7
P Axis: Str= 301.9 Plg= 2.7
T Axis: Str= 34.6 Plg= 42.7
P Horax: Azi= 302.6 Size=-0.997
T Horax: Azi= 32.6 Size= 0.539
Hor Dev Stress= 0.768 Err= 0.000

Figure 2.1.5. Focal mechanism solution from forward waveform modelling for a magnitude 2.1 event located within the NORSAR array. This figure illustrates the application of the modelling technique as applied to the NORSAR recording of an event at a distance of 40 km and to a frequency of 3 hz. The *left* frame shows the vertical component of NORSAR short period data together with a synthetic seismogram calculated with the fault plane solution from the *right* frame constrained by the first motion data.

2.2 Topographic effects on arrays and three-component stations

An analysis of the location capabilities of NORESS and ARCESS, and of the 3-component stations within the arrays, leads to the following conclusions concerning 3-component slowness solutions for P waves: (1) There is a relatively large scatter in the solutions for events from the same source region, and (2) there are significant differences between the solutions at the different stations. A third result is common for both array- and 3-component solutions: (3) There are signicant anomalies in the slowness of P from particular source regions. For a proper evaluation of NORESS and similar arrays, it is important to understand the cause of these observational phenomena. In this work we have analyzed topographic effects by comparing slowness solutions for P from explosions in 3 different source regions: near Leningrad, in E. Kazakh, and near Blåsjø in S.W. Norway.

Slowness analysis

A unified approach to slowness analysis with arrays and 3-component stations is possible by expressing solutions in terms of a covariance matrix C (e.g., Esmersoy *et al*, 1985). Here we introduce C as a function of slowness s by phase shifting the signals:

$$C_{nm}(\mathbf{s}) = \int F_n(w,\mathbf{s})F_m^*(w,\mathbf{s})dw/2\pi \qquad (1)$$

where

$$F_n(w,\mathbf{s}) = F_n(w)\,exp(iw\mathbf{s}.\mathbf{x}_n)$$

and F_n is the Fourier spectrum at channel n. Using C of eq. (1), the generalization of conventional beamforming is given by the normalized response

$$P(\mathbf{s}) = \mathbf{g}^\dagger C\mathbf{g}/\{|\,\mathbf{g}\,|^2\,tr C\} \qquad (2)$$

where $\mathbf{g}$ is the predicted displacement vector for slowness s. The generalization (2) can be interpreted as a matched filter since the response P depends on our choice of matching the covariance matrix C:

$$\mathbf{g}^\dagger C\mathbf{g} = tr(C\,G) \quad \text{with} \quad G = \mathbf{g}\,\mathbf{g}^\dagger$$

Thus for a 1-component array: $\mathbf{g}^T = (1,\ldots,1)^T$, and for a 3-component sensor: $\mathbf{g}^T = (g_x, g_y, g_z) = $ displacement vector. The latter is a function of slowness s, and the surface interaction must be taken into account. On this account we may expect 3-component slowness solutions to be relatively sensitive to the choice of near-surface model. It is possible to extend the procedure to a generalization of optimum beamforming. For example, the normalized response of the maximum likelihood method is

$$P'(\mathbf{s}) = \{\mathbf{g}^\dagger C^{-1}\mathbf{g}\}^{-1}\,|\,\mathbf{g}\,|^2\,/tr C \qquad (3)$$

15

Although eq. (3) leads to solutions with apparently higher resolution, the solutions are less stable and for location purposes stability is more important. Hence we will proceed the analysis based on eq. (2).

The Leningrad events

Figure 2.2.1 shows a typical 3-component record at NORESS from a mining explosion near Leningrad. Five such events were recorded with good signal-to-noise ratio, and Figure 2.2.2 summarizes both the array slowness solutions and the 3-component solutions for 4 stations within NORESS. Standard error bars indicate the scatter of solutions for the 5 events. Error bars of 3-component solutions are given for only one station, but the scatter for the other stations is similar. The theoretical results included in Figure 2.2.2 will be discussed later. The 3-component slownesses show a relatively large scatter, both of solutions at different stations for the same event and of solutions for different events at the same station. These solutions take into account wave interaction with a plane surface. An obvious extension is to include the effect of surface topography.

Interaction with surface topography

The usual correction for surface topography implies a time correction for elevation, and possibly a particle motion correction for surface slope. These corrections are consistent with geometrical ray theory, which requires that topographic relief be smooth on the scale of a wavelength. However, the topography of the NORESS area is not smooth on the scale of the relevant wavelengths ($\sim$ 2 km), and wave scattering effects may be important. The same is true for the ARCESS area. To evaluate the scattering, we have applied a perturbation method where the solution is obtained recursively in wavenumber space (Doornbos, 1988). For the present purpose we need the surface displacement $\mathbf{u}(x, y)$. The required perturbation series is then

$$\mathbf{U}(k_x, k_y) = \sum_{n=0}^{\infty} \mathbf{U}^{(n)}(k_x, k_y) \tag{4}$$

where $\mathbf{U}(k_x, k_y)$ is the Fourier transform of $\mathbf{u}(x, y)$, and $\mathbf{U}^{(n)}$ is a function of $\mathbf{U}^{n-m}$, $1 \leq m \leq n$, of the surface topography $f(x, y)$, and of the surface gradients $\partial f / \partial x$, $\partial f / \partial y$. The zeroth order term $\mathbf{U}^0$ gives the conventional free surface response for a plane, the first order term $\mathbf{U}^1$ includes the Born approximation, and the higher order terms account for multiple scattering.

We have synthesized the free surface response at NORESS in the signal bandwidth (2-4 Hz), assuming the incident wave direction is given by the array slowness solution. We then applied the method of equation (2) to the 3 components of surface displacement, to obtain theoretical slowness solutions for the 3-component station sites. The results are included in Figure 2.2.2. These results explain about half of the observed anomalies. We speculate that shallow subsurface structure may enhance the surface topographic effect. The results represent a weighted

integral over the bandwidth 2-4 Hz, but single frequency solutions give a significant variation with frequency. This is consistent with the notion of response by a rough surface as an interference pattern. Thus, different signal spectra from the same source region may lead to different slowness solutions, which might explain the scatter of solutions at a single station.

E. Kazakh events

Teleseismic P waves from recent nuclear explosions in E. Kazakh have been recorded both at NORESS and ARCESS. The P wave spectra from all events are similar at NORESS, but at ARCESS we can distinguish two groups of events. The spectra within a group are similar, but there are significant differences between the two groups. Representative spectra at ARCESS are shown in Figure 2.2.3, and average slowness solutions for each group are plotted in Figure 2.2.4 (a and b). There is a slight difference between the array slowness solutions, but there is a large difference between the 3-component solutions for the two groups. We have also plotted the theoretical slowness solutions for the 3-component station sites. The assumed signal bandwidth was 0.9-2.5 Hz for the "high-frequency" group of events, and 0.9-1.6 Hz for the "low-frequency" group. The results suggest that the surface topography at ARCESS explains slightly less than half of the observed anomalies. It is also clear that the slowness results for the two spectra are rather different in accordance with observations. This supports the explanation that the often significant variation of 3-component slowness solutions for signals from events in the same source region can be related to differences in the signal spectra.

Blåsjø events

We have analyzed in some detail the NORESS records of Pn from a suite of 6 mining explosions in the Blåsjø area in S.W. Norway. The mining site is about 300 km from NORESS in an azimuth direction of about 240°. A record section for one of these events with a plot of slowness as a function of time is shown in Figure 2.2.5. Slowness and azimuth of the first arrival are consistent with Pn in a one-dimensional crust-mantle model (e.g., Menke and Richards, 1980). However, it can be seen that the first arrival is relatively weak. In fact, this arrival is easily missed for small events, whence Pn is often associated with the dominant part of the wave train. The dominant part about 0.5-0.6 seconds after the first arrival has a consistent slowness and azimuth anomaly for all events. Slowness solutions as a function of frequency as summarized in the slowness/azimuth spectrum of Figure 2.2.6 show that the anomaly is related to the frequency range 2-4 Hz; this is also the range where the signal has its maximum energy. The nearly plane wavefront indicates that the anomaly cannot be generated near the surface, and it is suggested that these "Pn" waves are actually the result of scattering at depth. From the measured slowness and time delay, the scattering source is constrained to be within the depth range of the Moho (30-40 km). Hence the observational results are consistent with scattering by topographic relief of

the Moho. An interesting geological aspect is that the inferred location of the proposed topographic feature coincides with the border of the Oslo Graben.

Scattering by Moho topography

Scattering will of course affect all waves interacting with a rough Moho discontinuity. However, the scattered waves usually arrive in the coda of a relatively strong primary wave. In contrast, the first arriving Pn is relatively weak due to the small coefficient of refraction through the Moho, and scattering due to topography of the boundary may dominate the wave train.

To illustrate these concepts, we have calculated generalized transmission coefficients for a rough Moho. In analogy to equation (4) for the displacement vector. we introduce a recursive solution for the vector of scattering coefficients:

$$\mathbf{B}(k_x, k_y) = \sum_{n=0}^{\infty} \mathbf{B}^{(n)}(k_x, k_y) \tag{5}$$

The components of $\mathbf{B}^{(no)}$ are just the plane wave transmission coefficients for a plane interface. From the components of $\mathbf{B}$ we can calculate the energy flux for any wave type. Figure 2.2.7 shows the energy flux of P transmitted upward through a rough Moho, as a function of incident P below the boundary. The topography here is characterized by a correlation length of 5.6 km and an average height of 1 km, and the wave frequency is 3 Hz. Two modes of scattering are shown: (1) The specular flux E^o in the direction defined by the plane wave-plane interface concept. The specular flux through a rough interface is reduced with respect to the flux through a plane. (2) The diffuse flux E^{sc} due to multiple scattering in all upward directions. E^{sc} does not exist for a plane interface. The figure illustrates well the sharp increase of the ratio E^{sc}/E^o as the slowness approaches the critical value corresponding to Pn, thus supporting in a qualitative way the scattering model for propagation of this wave. The results suggest that a careful calibration is needed before using this phase for event location and velocity determination purposes.

D.J. Doornbos
E. Ødegaard, Univ. of Oslo
T. Kværna

References

Doornbos, D.J. (1988): Multiple scattering by topographic relief with application to the core-mantle boundary, *Geophys. J.*, 92, 465-478.

Esmersoy, ' V.F. Cormier and M.N. Toksöz (1985): Three component array processing. In: *The VELA Program*, ed. A.U. Kerr, DARPA.

Menke, W.H. and P.G. Richards (1980): Crust-mantle whispering gallery phases: A deterministic model of teleseismic Pn wave propagation, *J. Geophys. Res.*, 85, 5416-5422.
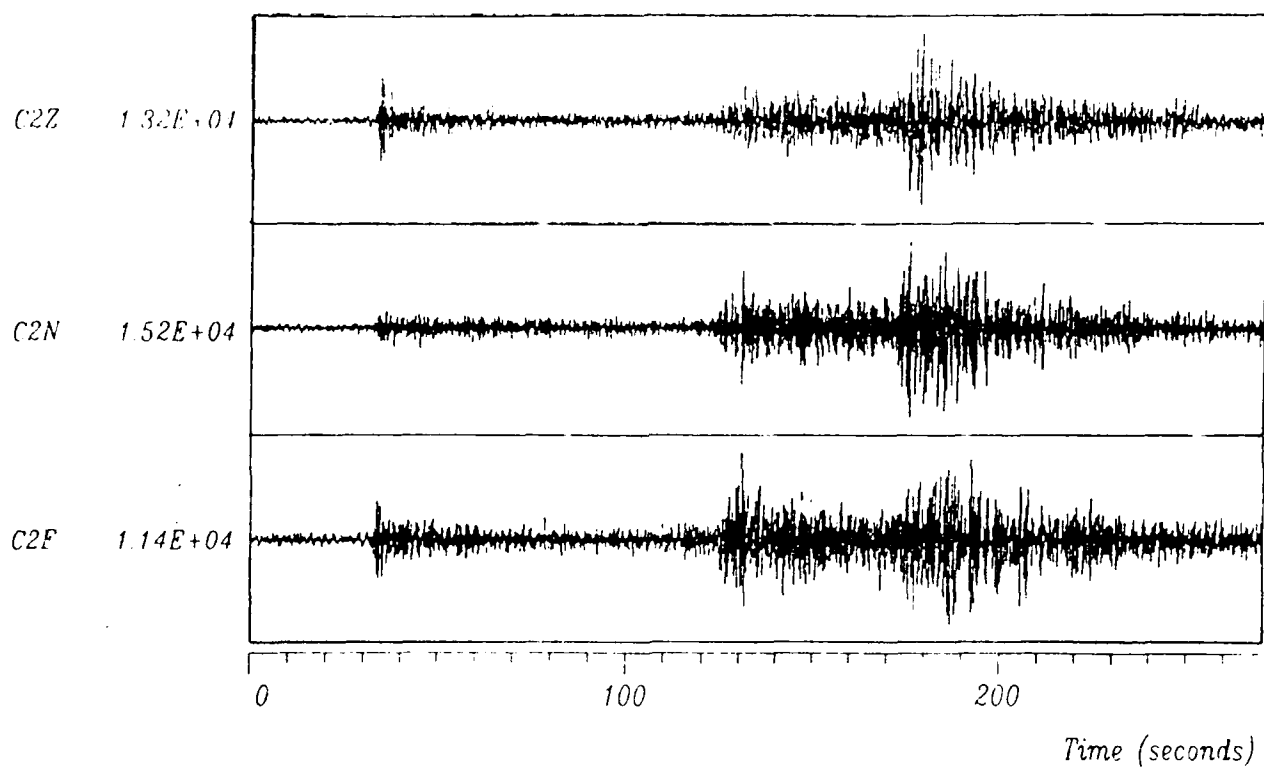
Fig. 2.2.1. Typical three-component NORESS records from event in Leningrad region. Scaling factors of different components are shown to the left.
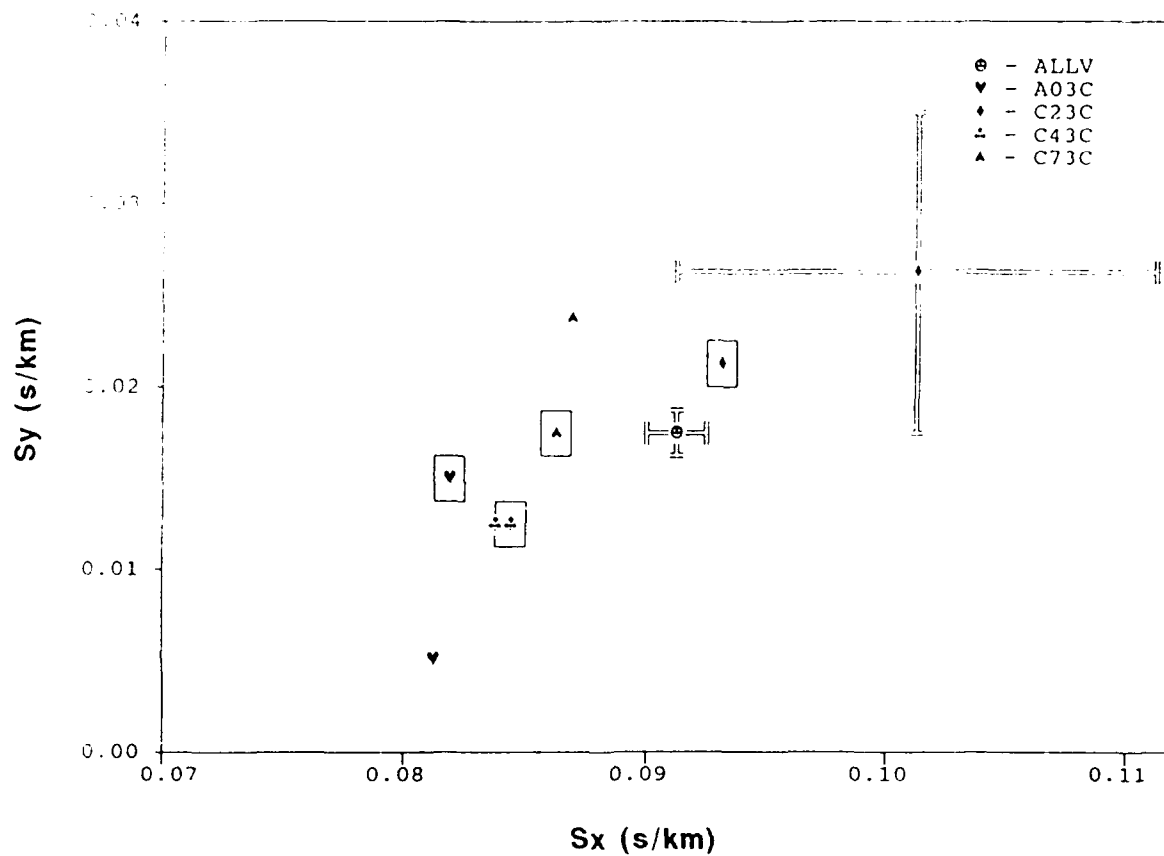
Fig. 2.2.2. Slowness solutions at NORESS. Average over P from 5 events near Leningrad. Array solution (ALLV) with standard error bars. Three-component solutions at the indicated sites, with standard error bars for site C2. Theoretical solutions including response to surface topography are framed.
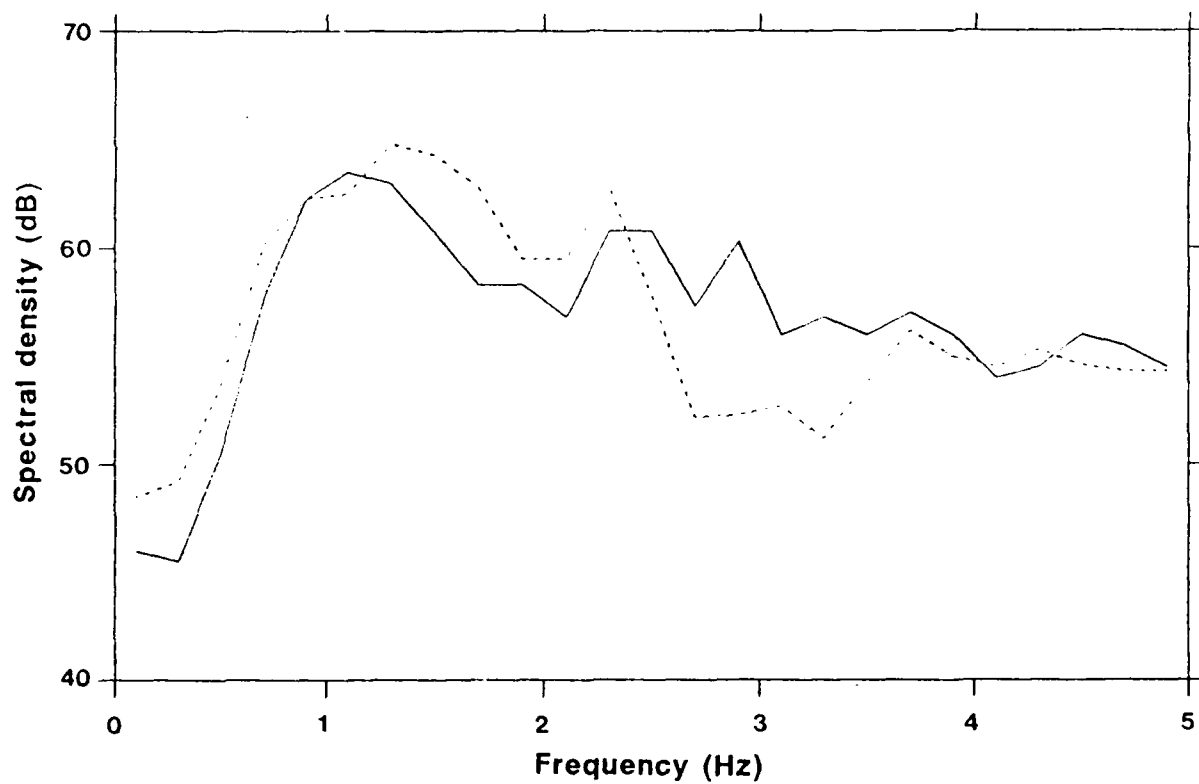
Fig. 2.2.3. P wave signal spectra at ARCESS from nuclear explosions in Kazakh.
--- : from group A (high-frequency signals).
——— : from group B (low-frequency signals.)
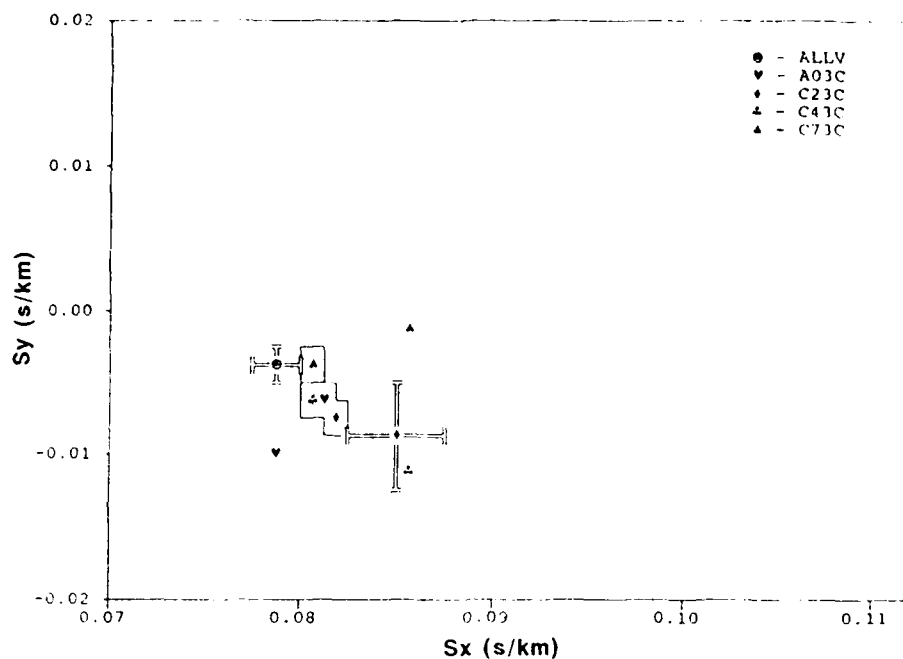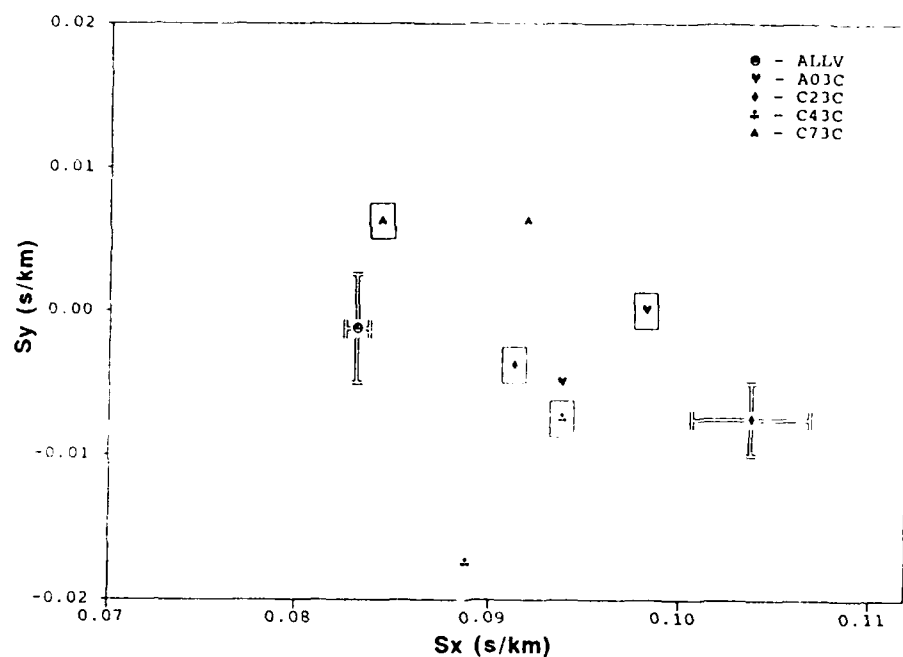
Fig. 2.2.4. Slowness solutions at ARCESS. Details as in Fig. 2.2.2.
a. Average over 4 events from group A in Kazakh.
b. Average over 5 events from group B in Kazakh.
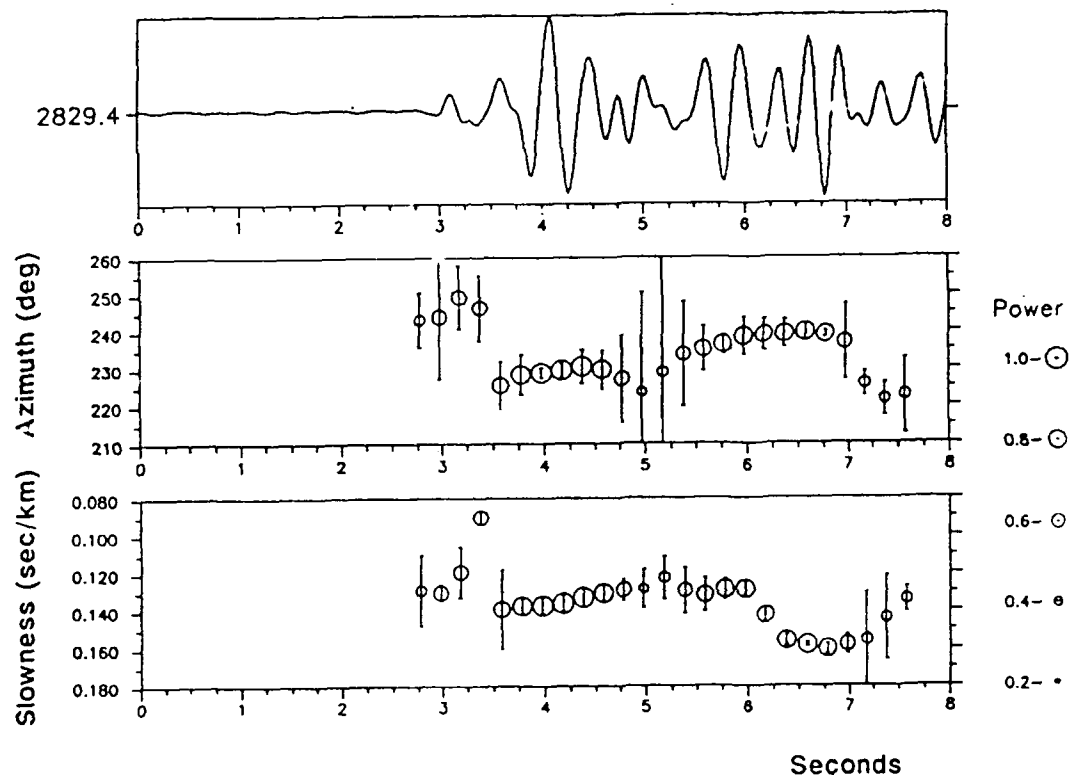
Fig. 2.2.5. NORESS record of Pn from an explosion in the Blåsjø area. The top trace is a single channel seismogram. Array solutions of slowness and azimuth as a function of time are shown below. The symbol size in the plot indicates the relative signal power.

24
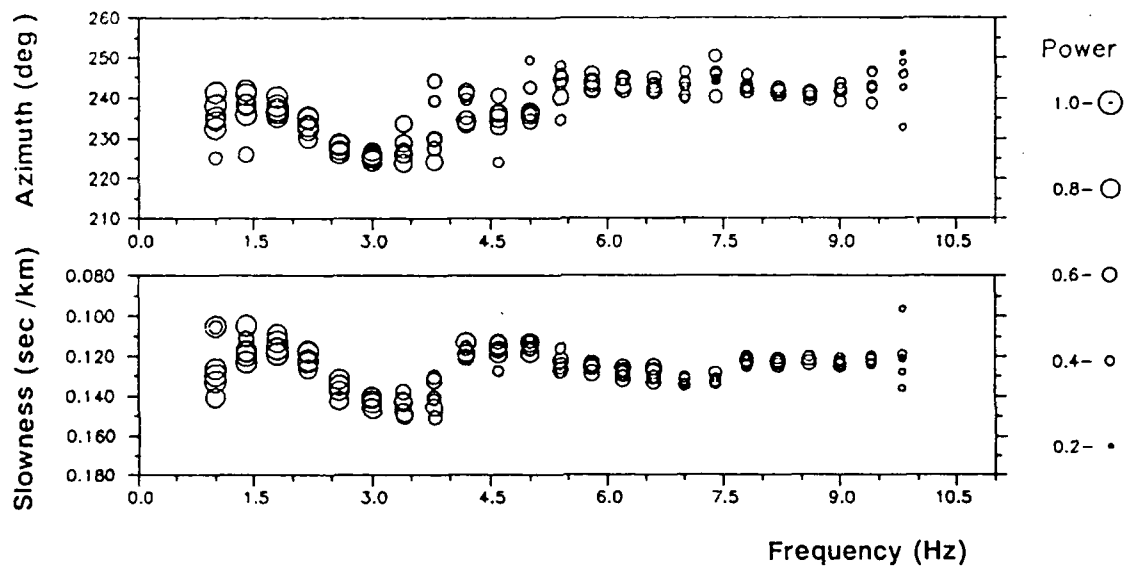
Fig. 2.2.6. Slowness and azimuth solutions of Pn as a function of frequency, from 6 explosions in the Blåsjø area. The symbol size indicates the relative signal power.
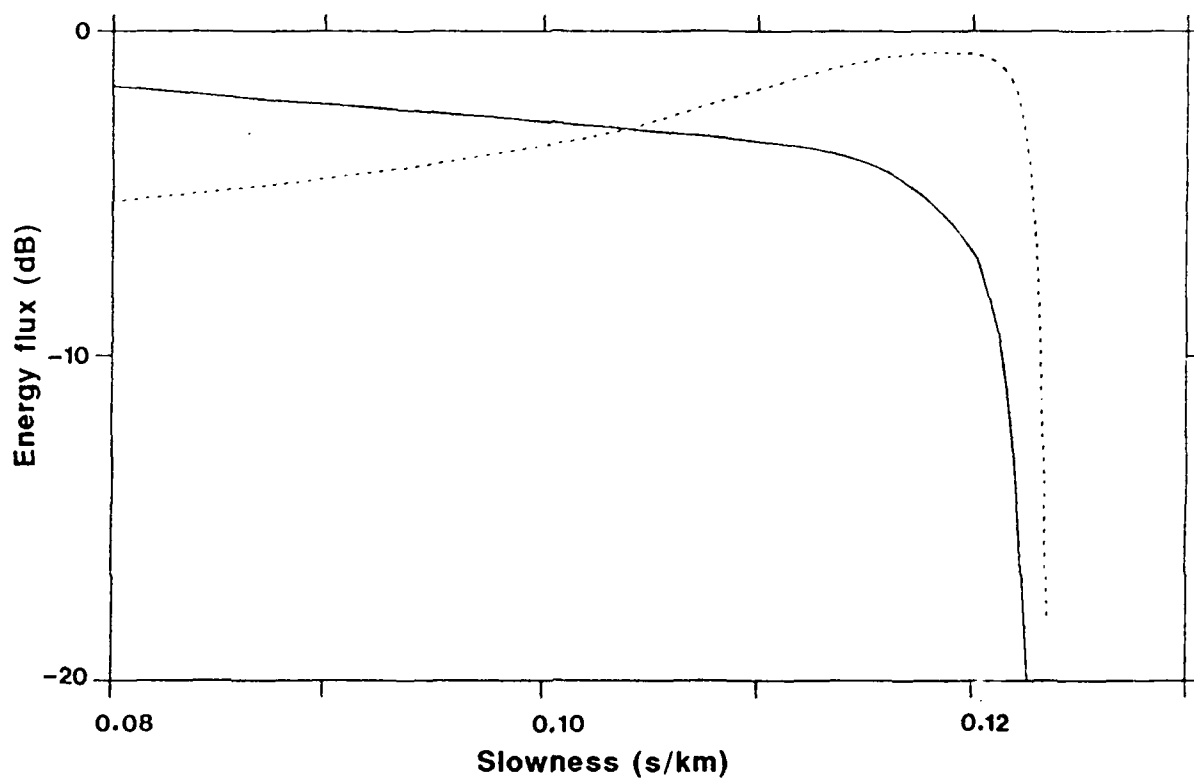
Fig. 2.2.7. Energy flux at 3 Hz through rough solid-solid interface with the velocity-density structure $v_p^{+/-} = 6.8/8.1$ km/s, $v_s^{+/-} = 3.7/4.5$ km/s, $\rho^{+/-} = 2.9/3.4$ g/cm^3. The boundary roughness is characterized by an average height of 1 km and a correlation length of 5.6 km. The scattered flux is upward through the boundary.

——— : specular direction; — — — : integrated diffuse flux.

2.3 Local magnitudes and regional wave attenuation

Introduction

The research conducted during the last year within the field of regional wave attenuation and local magnitudes has been organized as part of a more long term plan, with the following done so far:

- Establishment of a large data base of regional records, stored in a common format

- Development of analysis tools and strategies, and preliminary analysis of data

In the following, we will describe each of these subjects in more details.

Data base of records

For a long time, the network of seismic stations in Norway was limited to a few (2-4) conventional analog stations, and from 1970, the NORSAR array. Then, between 1980 and 1983, the regional Southern Norway Seismic Network (SNSN) was in operation, the Western Norway Seismic Network (WNSN) started recording in late 1984, and the Northern Norway Seismic Network (SEISNOR) in early 1987. With NORESS (1985) and ARCESS (1987) in addition, the whole country and surrounding areas are therefore now quite well covered.

It is being recognized now, more and more, that well-calibrated magnitude scales are quite important in very many seismological problems and applications. This is obviously true for problems related to detectability and yield estimation, but also to wave attenuation where magnitude in some cases is an important scaling parameter. It is also being recognized that the development of a new regional magnitude scale requires a very thorough development of its wave attenuation terms, and that this requires large amounts of observed data in order to be sufficiently reliable. The data situation described above for Norway makes this the right time for pursuing these goals.

To this end, we have undertaken a major effort in terms of establishing a large data base of regional earthquake records, later to be used in the investigation of a variety of seismological problems. The data collected so far consists of more than 200 earthquakes and more than 1000 individual records, with magnitudes in the range M_L 1.7-5.3 and epicentral distances in the range 10-2000 km. All of these records have been converted to a common format, convenient for interactive analysis by program packages which already include all necessary system response information.

27

For the records selected, all epicenters, recording stations and ray paths are shown in Fig. 2.3.1, while the magnitude-distance distribution is shown in Fig. 2.3.2. It should be noted here that some of these records (near-field, large magnitudes) are clipped, while others (far field, low magnitudes) may be too much affected by noise.

Analysis strategies

In following Richter (1935; 1958), the local magnitude M_L is defined as (see also Boore, 1989):

$$M_L = log A - log A_0 + S \tag{1}$$

where A is measured amplitude (0-p) in mm on a Wood-Anderson seismometer recording, S is a station correction, and

$$- log A_0 = a \cdot log(\Delta/100) + b \cdot (\Delta - 100) + 3.0 \tag{2}$$

where a and b are coefficients and Δ is epicentral distance.

With no station correction, this definition gives $M_L = 3.0$ for $A = 1$ mm at a distance of 100 km. Richter's original A_0 (attenuation) values, developed from a very small data base of Wood-Anderson seismometer recordings from southern California, are surprisingly correct, as demonstrated recently by Bakun and Joyner (1984) for central California and by Hutton and Boore (1987) for southern California.

In developing a new M_L scale for a different region, it is first of all necessary to develop a new attenuation relationship for the area, in terms of the coefficients a and b in equation (2). A problem in this respect is that regional differences between attenuation at 100 km makes it very questionable to tie the two scales together at this distance. In using a shorter distance, such as 10-20 km, we then on the other side run into a problem caused by the fact that Richter's A_0 values are more poorly defined there.

One way to solve this problem has been suggested by Hutton and Boore (1987), who developed new attenuation relations for southern California from a very large data base. Using their A_0 values, which are identical to Richter's at a distance of 100 km, a magnitude 3.0 earthquake should be recorded with an amplitude of 10 mm at a reference distance (Δ_{ref}) of 17 km. This distance is more satisfactory for anchoring purposes, under the condition that our local attenuation function can be evaluated with a sufficient precision down to that distance. If that is not the case, a larger Δ_{ref} must be chosen.

This leads to the following expression for A_0:

$$- log A_0 = a \cdot log(\Delta/\Delta_{ref}) + b \cdot (\Delta - \Delta_{ref}) + K(\Delta_{ref}) \tag{3}$$

where $K(\Delta_{ref})$ is determined from the A_0 values of Hutton and Boore (1987);

e.g. $\Delta_{ref} = 17$ km gives K = 2.0. A regression analysis should then be aimed at solving for the parameters a, b, S and M_L in equations (1) and (3).

The collected data will be read from the data base and checked manually for noise level, clipping, etc. Fig. 2.3.3 shows in this respect a panel of records from an M_L 3.1 earthquake on 17 September, 1988, with epicentral distances from 176 to 1308 km. The stations include three from SEISNOR, NORESS and two from WNSN, and serves as a good illustration of the usefulnes in mixing records from different recording systems.

The usable records will then be corrected for instrument response (in frequency domain) in order to get true ground motion spectra as shown in Fig. 2.3.4, or ground motion time series, in the cases when those are needed. Simulated Wood-Anderson recordings are then established by applying an appropriate high pass filter (2-pole hp at 1.25 Hz, most conveniently applied also in frequency domain), and the resulting time series is then plotted (on the screen) for manual picking of maximum amplitude. These amplitudes are then used regressively by combining equations (1) and (3) to give

$$log A_{ij} = -a \cdot log(\Delta_{ij}/\Delta_{ref}) - b \cdot (\Delta_{ij} - \Delta_{ref}) - \sum_{k=1}^{N_s} S_k \delta_{kj} + \sum_{l=1}^{N_e} M_{Ll} \delta_{il} - K(\Delta_{ref}) \quad (4)$$

where

A_{ij} = simulated Wood-Anderson amplitude of earthquake i at station j

δ_{ij} = Kronecker's symbol (=1 if i=j, otherwise 0)

N_s = number of stations

N_e = number of events

The parameters to be determined regressively are a, b, S_k and M_{Ll} representing the geometrical spreading, attenuation, station correction and magnitude, respectively.

The true ground motion time series and associated Fourier spectra obtained from the data base serve as important subsets of data suited for further wave attenuation research. Such efforts should emphasize the interrelation of geometrical spreading and anelastic attenuation in the computation of wave attenuation, possible local and regional differences in wave attenuation, and also possible azimuthal effects. In contrast to the attenuation terms in the M_L inversion, the terms here can be evaluated as functions of frequency (Dahle et al, 1989).

Preliminary results

In the section above, we have outlined a procedure for simultaneous inversion of Wood-Anderson amplitudes vs. epicentral distance in order to estimate M_L magnitudes, station corrections, geometrical spreading and anelastic attenuation. This can be done at the same time or through a multi-step regression analysis. In order to test the stability of our planned procedure we selected a few representative recordings as shown in Table 2.3.1, including 8 events and 35 records. The reference distance in this case has been 100 km, the estimated magnitudes are given in Table 2.3.1, while the station corrections are shown in Table 2.3.2.

The coefficients a and b in equation (4) are as follows:

a (geometrical spreading) : 0.70

b (anelastic attenuation) : 0.0010

These results are very encouraging in that we for all of the 21 estimated coefficients get reasonable values using only 35 independent observations. In general, however, we must expect this kind of analysis to be more unstable than shown here, and that therefore the various restrictions for the different parameters should be considered closely, in addition to the possibilities for a multi-step regression analysis. The resulting magnitude formula would read as follows (ignoring the station corrections):

$$M_L = logA + 0.70 \cdot log\Delta + 0.001 \cdot \Delta + 1.5 \qquad (5)$$

We emphasize that these results are preliminary and intended only for test purposes.

A. Alsaker
L.B. Kvamme
A. Dahle
H. Bungum

References

Boore, D.M. (1989): The Richter scale: its development and use for determining earthquake source parameters, *Tectonophysics*, **166**, 1-14.

Bakun, W.II. and W.B. Joyner (1984): The M_L scale in central California, *Bull. Seism. Soc. Am.*, **74**, 1827-1843.

Dahle, A., II. Bungum and L.B. Kvamme (1989): Attenuation models inferred from intraplate earthquake recordings. Submitted for publication.

Hutton, L.K. and D.M. Boore (1987): The M_L scale in southern California, *Bull. Seism. Soc. Am.*, **77**, 2074-2094.

Richter, C.F. (1935): An instrumental earthquake magnitude scale, *Bull. Seism. Soc. Am.*, **25**, 1-32.

Richter, C.F. (1958): *Elementary Seismology*, W.II. Freeman and Co., San Francisco, California, 758 pp.

Earthquake	No. of obs.	Old M_L	New M_L
1986 Feb 5	1	4.8	4.92
1986 Oct 26	1	4.4	4.44
1987 Oct 31	3	3.6	3.82
1987 Nov 1	6	3.1	3.18
1987 Nov 3	5	2.3	2.39
1988 Jan 23	10	3.4	3.35
1988 Jan 31	6	3.8	3.65
1988 Aug 8	3	5.2	5.20

Table 2.3.1. Earthquakes used in testing inversion procedure for M_L determinations, with number of records for each event, old M_L (from current formula), and new M_L (from inversion).

Station	No. of obs.	Correction
NRS	8	- 0.02
MOR1	1	0.12
FRS	5	- 0.02
MOL	4	- 0.09
LOF	2	0.17
TRO	4	0.20
KTK1	3	- 0.18
SUE	2	0.05
HYA	2	- 0.12
ODD1	2	- 0.11
KMY	2	- 0.02

Table 2.3.2. Station corrections from testing inversion procedure for M_L determinations, with station name in column 1 and number of records in column 2.
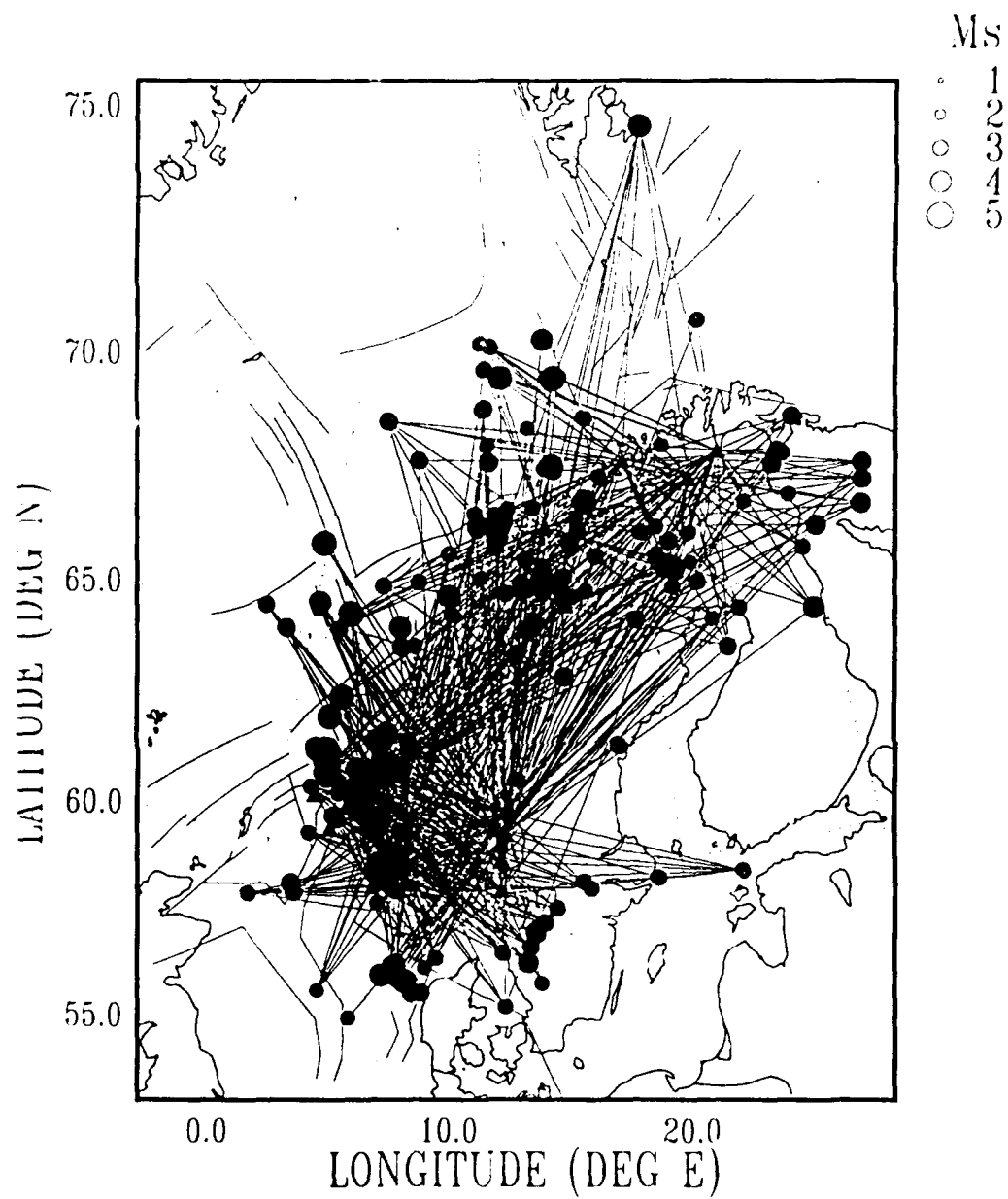
Fig. 2.3.1. Locations of all events in the data base, connected with ray paths to each of the stations which have contributed with recordings.
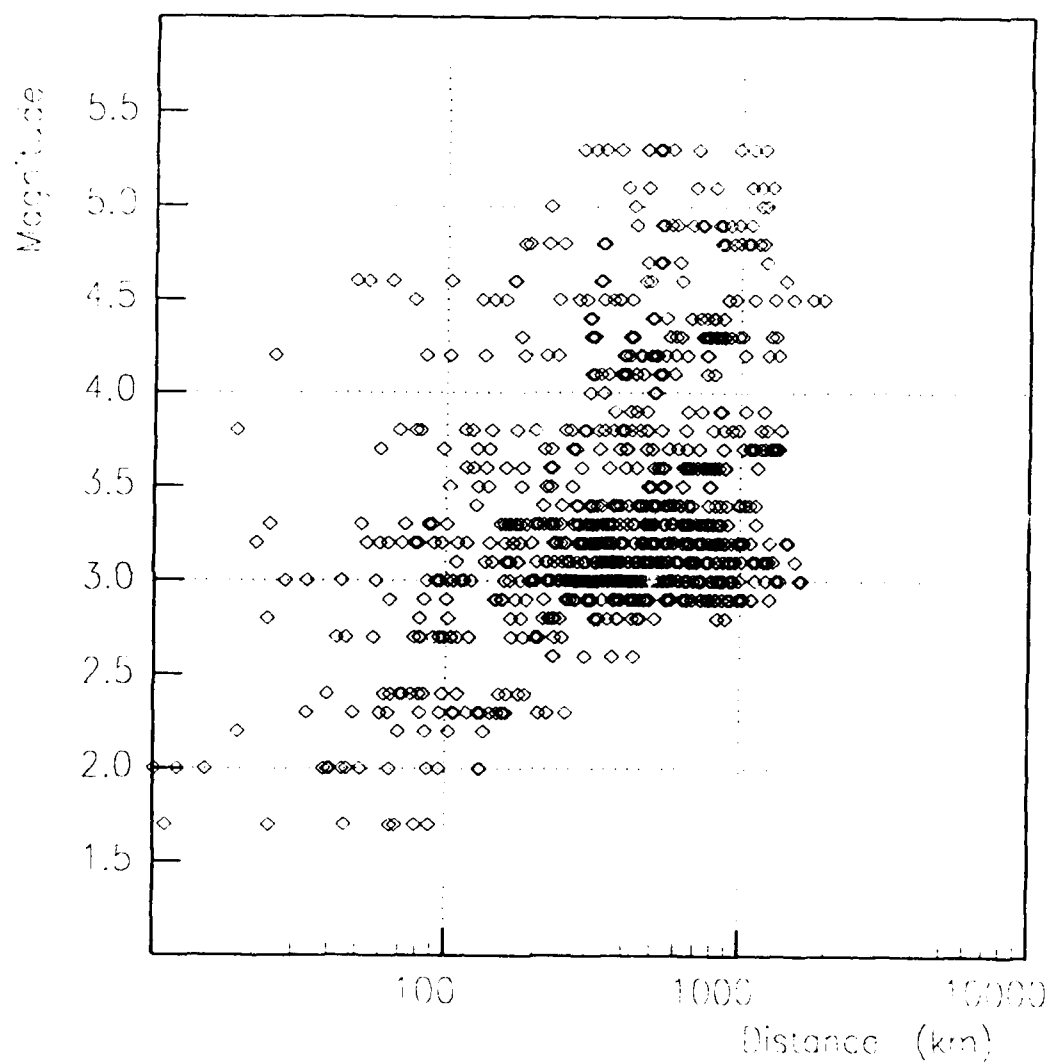
Fig. 2.3.2. Magnitude-distance distribution for all of the data in the data base (203 events, 1028 records).
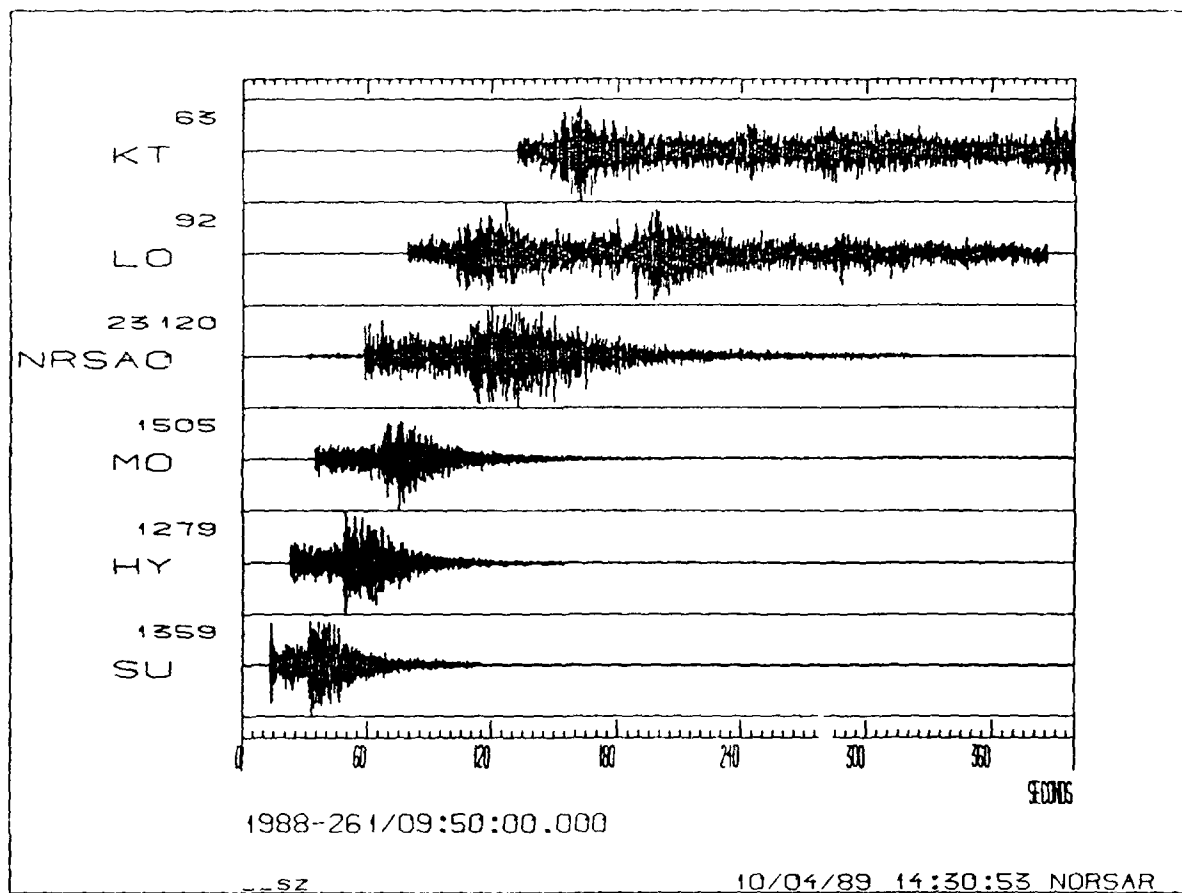
Fig. 2.3.3. Recordings at six stations from an M_L 3.1 earthquake on 17 September 1988, located at 61.42°N, 1.57°E. The two closest stations are from WNSN, while the others are from NORESS (NRS), and from SEISNOR. The epicentral distances are SUE 176, HYA 249, MOL 338, NRS 543, LOF 937 and KTK 1308 km, respectively.

35

MOL 50 s S-record 1338 k
1988 261/ 9:51: 4.000
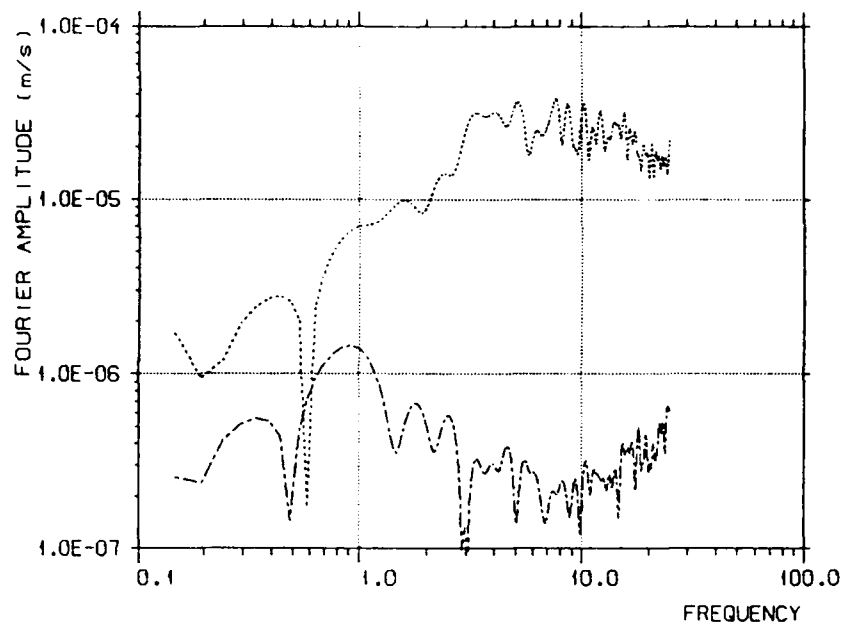
KTK 85 s S-record 1308 k
1988 261/ 9:54:27.680
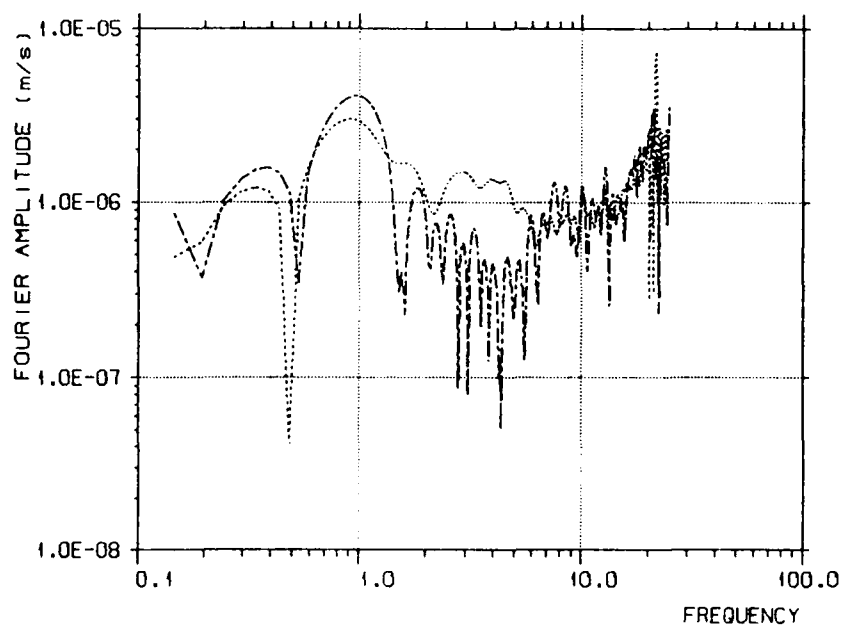
Fig. 2.3.4. Fourier acceleration ground motion L_g spectra for the recordings at the stations MOL and KTK in Fig. 2.3.3, plotted together with similar estimates from the preceding noise. It is seen that KTK (recording an M_L 3.1 earthquake at a distance of 1308 km) has a positive signal-to-noise ratio only around 2-6 Hz.

2.4 A generalized beamforming approach to real time network detection and phase association

Introduction

The objective of this study is to investigate methods for multi-array detection, phase association and location, using as primary data sources the three regional arrays (NORESS, ARCESS, FINESA) in Fennoscandia. The emphasis is on approaches which are suitable for incorporation in an expert system environment. As part of this effort, the problem of continuously monitoring the regional seismic noise field is also addressed, with the purpose to obtain a quantitative assessment of the upper limit of magnitudes of seismic events that would go undetected by such a network.

A more exhaustive treatment of the subject of this contribution is offered in our Scientific Report No. 1 under this contract (GL Report Number: GL-TR-89-0171), which will also appear in the December 1989 volume of the *Bulletin of the Seismological Society of America*.

General approach

In the processing of seismic network data, individual phase detections corresponding to the same seismic event must be properly associated and grouped together. This is today usually done starting with an initial trial epicenter and then applying various search strategies supplemented by combinational techniques.

This paper presents, and gives examples of application of, a method for associating phase detections from a network of stations, which is analogous to the conventional delay-and-sum beamforming commonly applied in array detection processing. A number of beams are steered to a predefined grid of aiming points in a geographical space. Each beam has an associated set of time delays, where each delay corresponds to the predicted travel time for a given phase at a given station.

We assume that the data of each network station is initially subjected to a detection processing procedure, whereby a list of phase detections and attributes is generated. The beamforming process, for a given beam, at time T, can be described as looking for a pattern of detections/non-detections that matches the predicted pattern for a hypothetical event with origin time T and location within the beam region. The actual beam value is derived from probabilistic considerations, and in essence describes how well the observed pattern matches the prediction. By moving along the time axis, we thus obtain a beam trace that can be subjected to standard threshold algorithms for detection. The process can be supplemented by various individual "quality of fit" measures calculated at each time point.

After processing individual beams as described above, a grouping/reduction process is applied to the set of all beam detections to eliminate side lobe detections. This then results in an event list, comprising origin times, locations and a list of associated phases. Further refinement can then be achieved by standard techniques for accurate hypocenter determination, magnitude computation, final consistency check, etc.

The generalized beamforming approach also provides a convenient tool to monitor continuously the seismic noise field associated with a given beam. An application of particular interest in a monitoring situation would be to calculate, at each step in time, upper confidence limits for the magnitude of non-detected events for each beam. This would be useful to obtain a realistic assessment of actual network detection capabilities, at any given point in time. The paper presents an example of practical application of this approach.

Regional phase association

The method has been applied to a data base comprising 24 hours of recordings from the regional arrays NORESS, ARCESS and FINESA, with a beam deployment covering Fennoscandia and adjacent areas.

A RONAPP-type detector was first applied to each array individually, using the broad-band F-K method to obtain phase velocity and azimuth for each detected phase. The resulting detection lists then provided the input to the network processor.

The beam grid used for network processing is shown in Figure 2.4.1, and comprises altogether 121 aiming points, approximately equally spaced. Typical distance between aiming points is 150 km.

In the network beamforming process, a simple model of assigning 0/1 probabilities to individual phases at each station was used. We required that estimated phase velocities, azimuth, dominant frequency and arrival times fall within predefined ranges for a phase detection to be accepted for a given beam. These tolerance ranges are specified in Table 2.4.1. Note in particular that only very general criteria are applied, and we have made no attempt to optimize performance by regionalization.

With this simplified model, the network beamforming process in practice was reduced to, for each beam and each time T, counting the number of phase matches for a hypothetical event located in the beam region and having origin time T. The detection threshold was set equal to 2. Thus, all occurrences of two or more matching phase detections were flagged as potential events. A typical beam trace is shown in Figure 2.4.2.

A grouping procedure was then applied to the overall beam detection list. This was done by successively linking together entries in the beam detection list

in such a way that a new entry would be linked if it had at least one individual phase detection in common with a previous entry in the group. The maximum allowable duration of a group was set to 10 minutes (in practice, the longest duration was 7 minutes for this data set). In order to resolve obvious multiple events, groups were split up if two P-detections from the same array occurred with more than 30 seconds arrival time difference.

The results are summarized in Table 2.4.2. It is important to note that the total of 91 groups comprise *all* possible events that could be associated, given the station detection lists. Also, a scrutiny of the data shows that only 3 of these groups contain multiple events, all of these being small presumed mining explosions seen by one array only.

Some of the entries in Table 2.4.2, e.g., those generated from two secondary phases, are probably questionable seismic events, and even if real, may be impossible to locate accurately. An upper magnitude limit could be estimated for such events, in order to determine whether further detailed analysis is desirable. However, the large majority of the entries appear to correspond to real seismic events, and the grouping procedure facilitates the subsequent detailed analysis of the associated phases.

The network beamforming procedure gives an initial estimate of event location by selecting the "best beam" in each group. This is defined as the beam with the greatest number of associated phase detections, and if equality, the smallest average time residual of the detected phases. Since the initial beam grid is very coarse, we applied a beampacking algorithm for each detection group, using a grid spacing of 20 km in order to improve the location estimate.

The results of this automatic procedure are shown in Table 2.4.3 for those events for which independent location estimates were available. We note that the estimates are very consistent (median difference 40 km), and thus the beam results can be used as a reasonable first estimate of event location. For more accurate results, available techniques for accurate hypocenter location (e.g., TTAZLOC) should be used.

Continuous monitoring of upper event magnitude limits

As a second application of the generalized beamforming procedure, we now address the problem of monitoring the noise levels on each beam, and use this information to assess the size of events that might go undetected.

In formulating the approach, we consider a given geographical location, and a given "origin time" of a hypothetical event. Assume that N seismic phases are considered (there might be several stations and several phases per station).

For each phase, we have an estimate S_i of the signal (or noise) level at the predicted arrival time. For P-phases, S_i might be the maximum STA value (1 sec-

39

ond integration window) within ± 5 seconds of the predicted time. For Lg, S_i might be the average STA value over a 10-20 seconds window.

We assume that the network has been calibrated (or alternatively that standard attenuation values are available), so that magnitude correction factors (b_i) are available for all phases. Thus, if a detectable signal is present:

$$m_i = log(S_i) + b_i \qquad (i = 1, 2, \ldots N)$$

Here, m_i are estimates of the event magnitude m. Statistically, we can consider each m_i as sampled from a normal distribution (m, r). (A standard value of $r = 0.2$ seems reasonable for a small epicentral area.)

Let us now assume a "noise situation", i.e., that there are no phase detections corresponding to events at the given location for the given origin time.

We then have a set of "noise" observations a_i, where

$$a_i = log(S - i) + b_i \qquad (i = 1, 2, \ldots N)$$

If a hypothetical event of magnitude m were present, it would have phase magnitudes m_i normally distributed around m. We know that for each phase,

$$m_i < c_i \qquad (i = 1, 2, \ldots N)$$

Let us look at the function

$$f(m) = \text{Prob(all } m_i \leq a_i/\text{event magnitude } m)$$

For each phase

$$f_i(m) = \text{Prob}(m_i \leq a_i/m) = 1 - \Phi(\frac{m - a_i}{\sigma})$$

where Φ is the standard (0,1) normal distribution.

Thus, assuming independence,

$$f(m) = \prod_{i=1}^{N} f_i(m)$$

The 90 per cent upper limit is then defined as the solution of the equation $f(m) = 1 - 0.90$

It is important to interpret the 90 per cent limit defined above in the proper way. Thus, it should not be considered as a 90 per cent network detection threshold since we have made no allowance for a signal-to-noise ratio which would be

40

required in order to detect an event, given the noise levels. Rather, the computed level is tied to the actually observed noise values, and to the fact that any hypothetical signal must lie below these values. Our 90 per cent limit represents the largest magnitude of a possible hidden event, in the sense that above this limit, there is at least a 90 per cent probability that one or more of the observed noise values would be exceeded by the signals of such an event.

As an application of the method, we selected an area as shown in Figure 2.4.3 situated at similar distance from the three arrays. For each of the three arrays, one Pn beam and one Lg beam were steered to this location. The beam traces were filtered using the frequency bands 3-5 Hz (Pn) and 2-4 Hz (Lg). Magnitude calibration values (b_i) were obtained by processing previously recorded events of known magnitude (M_L) and at similar distance ranges, and then determining b_i values independently for Pn and Lg.

Based on these input traces from the three arrays, a network beam was then formed, using time delays for each phase that corresponded to the given location. Arrival time tolerances were set to $\pm$ 5 seconds for P-phases and $\pm$ 10 seconds for secondary phases. This is roughly consistent with a beam radius of 50 km as shown on the figure.

We chose to analyze a 3 1/2 hour interval during which four regional seismic events of $M_L > 2.0$ were reported in the Helsinki bulletin. No events were reported near the beam area in this period. Figure 2.4.4 shows 90 per cent upper magnitude limits as previously defined, plotted as a function of time. In this figure, only the Pn phase has been used, and the three arrays are shown individually and in combination (bottom trace).

It is clear from Figure 2.4.4 that when considering individual arrays only, there are several possible time intervals when relatively large events ($M_L \sim 2.0$ 3.0) might go undetected because of signals from interfering events. However, when the Pn phases are combined, these instances occur much more seldom.

Figure 2.4.5 shows a similar plot, but this time including both the Pn and the Lg phase for each array. Even on an individual array basis, this causes substantial reduction in the upper magnitude limits. For the combined plot (bottom trace of Figure 2.4.5), which takes into account all 6 Pn and Lg phases from the three arrays, we see that the upper limit is well below $M_L = 2.0$ for the entire time interval. Thus, we may conclude that, at the specified level of confidence, no event of $M_L = 2.0$ or higher occurred in the beam region during the time period considered.

Conclusions

With regard to phase association, the generalized beamforming technique provides an effective method to group all combinations of individual phase de-

41

tections that could possibly correspond to the same seismic event. At the same time, preliminary estimates of epicenter and origin time are obtained.

The primary importance of this would be to obtain a starting point for subsequent detailed interactive analysis aimed at precise determination of source parameters. In particular, expert system approaches (either script-based or rule-based) could be invoked at this stage. The advantage of applying the generalized beamforming as the first step is to reduce the amount of combinational processing that would be necessary otherwise. It is here noteworthy that the processing load when applying generalized beamforming increases in a linear fashion when the number of individual phase detections increase, whereas combinational possibilities tend to increase exponentially. While we have in this paper used only a three-array network, the extension to larger networks is clearly straightforward.

The application of the method to provide continuous monitoring of upper magnitude limits at specified beam locations provides a useful supplement to standard statistical network capability studies. In particular, this application would give a way to assess the possible magnitude of non-detected events during the coda of large earthquakes. In such situations, it would be appropriate to use global network data and include as many relevant phases as possible for each network station. For example, while an expected P phase at a given station may be obscured by the earthquake coda, later phases such as PcP or PP may be less influenced, and the noise level at their respective expected arrival times would therefore provide important information as to the size of possible undetected events.

As a final comment, we note that the approach presented here to upper limit magnitude calculation could be applied to extend the utililty of various discriminants, such as $M_s : m_b$. For small explosions, surface waves frequently are too weak to be observed at any station of the recording network. Obtaining reliable upper bound on M_s in such cases would expand the range of usefulness of this discriminant. In practice, an "upper bound" for single-station measurements has often been given as the "noise magnitude" at that station, i.e., the M_s value that corresponds to the actually observed noise level at the expected time of Rayleigh wave arrival. The proposed procedure will include this as a special case of a more general network formulation.

In future studies, we plan to investigate the application of more sophisticated probabilistic models in the generation of beam traces and the continuous extraction of features associated with the individual beams. Application to larger networks, including teleseismic monitoring using global network data, will also be considered.

Frode Ringdal
Tormod Kværna

	Phase Type				
	Pn	**Pg**	**Sn**	**Lg**	**Rg**
Distance interval[1] (km) for which a phase is accepted	160-3000	0-600	160-3000	0-2000	0-400
Maximum allowable deviation from predicted arrival time (s)	15	20	30	35	40
Maximum allowable azimuth deviation (degrees)	20	20	20	20	20
Acceptance limits for apparent phase velocity (km/s)	5.8-14	5.8-10	3.2-5.8	3.0-5.0	2.5-3.7
Acceptance limits[2] dominant frequency (Hz)	0.5-20	0.5-20	0.5-20	0.5-20	0.5-20

[1] For NORESS, the Rg phase is not included in the phase table

[2] For FINESA, a lower frequency limit of 0.9 Hz is used for all phases.

Table 2.4.1. Acceptance limits for parameters used in the network beamforming process.

		Number of phases for best beam in each group						
No. of phase groups:		2	3	4	5	6	7	8
NORESS only	18	13	4	1	0	0	0	0
ARCESS only	34	19	10	4	1	0	0	0
FINESA only	14	13	1	0	0	0	0	0
Two arrays	17	9	4	3	0	1	0	0
Three arrays	8	0	0	2	0	1	3	2
Totals	91	54	19	10	1	2	3	2

Table 2.4.2 Phase groups associated by the network beamforming procedures for a 24-hour interval.

Event No.	Date	Time	Network Lat.	Network Lon.	Mag. M_L	No. of phases	No. of arrays	Beamforming Lat.	Beamforming Lon.	'Error' (km)
1	88/03/17	08.40.25.0	57.73	11.03	2.5	7	3	57.9	10.4	39
2	"	08.46.18.7	58.07	11.36	2.6	6	2	57.9	10.8	36
3	"	09.07.10.3	58.08	11.43	2.7	8	3	57.8	10.8	47
4	"	10.21.23.0	69.60	29.90	2.9	8	3	69.6	30.5	23
5	"	10.27.20.0	59.20	27.60	2.3	4	2	59.5	27.5	34
6	"	10.46.21.0	59.20	27.60	<2.0	2	1	59.8	28.7	96
7	"	11.18.48.0	59.30	27.20	2.3	5	3	58.9	26.7	52
8	"	11.54.41.0	65.80	24.70	<2.0	5	1	66.6	24.4	89
9	"	11.57.57.9	60.57	8.36	1.8	2	1	60.6	8.1	14
10	"	12.02.36.0	59.40	28.50	2.1	3	2	59.5	28.2	20
11	"	12.42.22.9	59.78	10.76	2.3	3	1	59.5	10.0	52
12	"	14.13.14.0	58.33	6.28	2.4	4	1	58.0	6.1	38
13	"	14.21.08.0	60.90	29.40	2.3	3	2	61.3	29.1	47
14	"	14.33.48.3	59.06	5.88	2.2	2	1	58.9	3.3	144
15	"	18.58.08.1	59.68	5.57	3.2	7	3	60.0	5.7	36

Table 2.4.3. Location estimates obtained automatically from the beampacking procedure compared with independent network locations from the Helsinki and Bergen bulletins. Note the good consistency, especially for events with more than one detecting array.
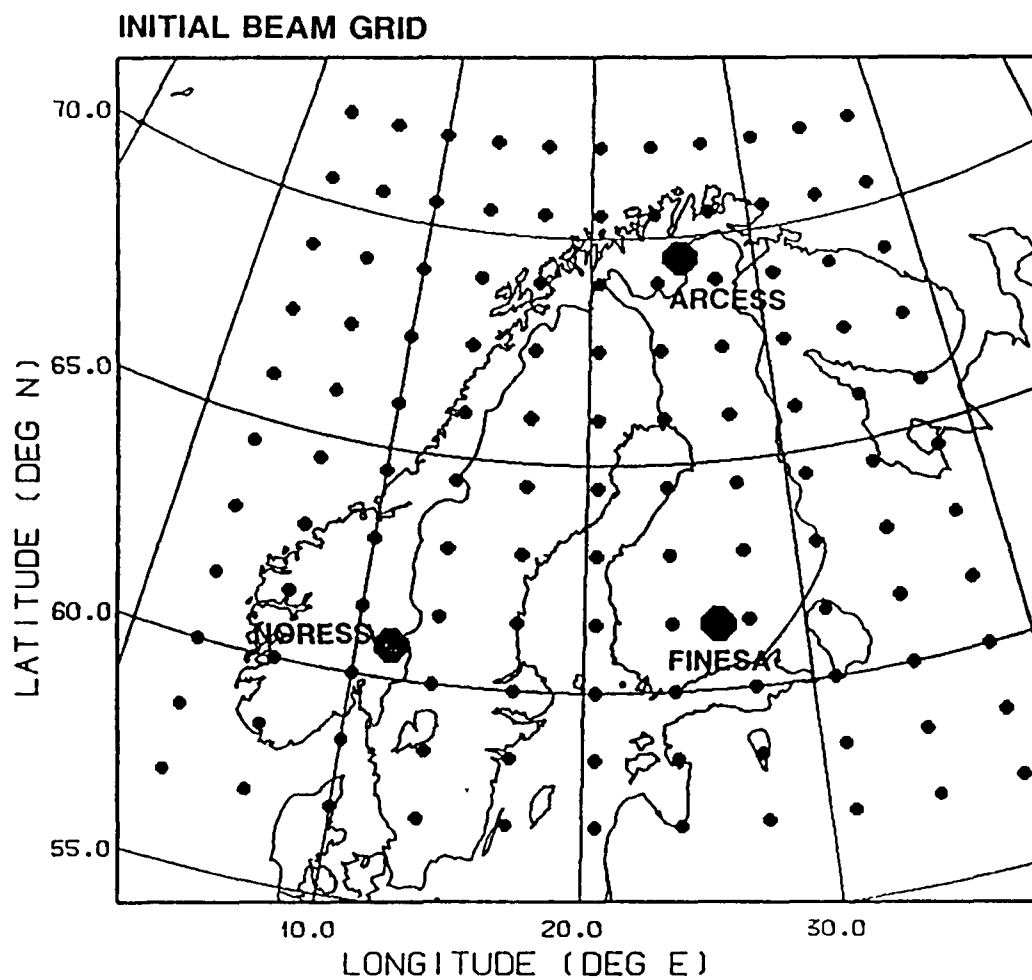
45

INITIAL BEAM GRID

Fig. 2.4.1. Beam grid used in the generalized beamforming procedure for the purpose of associating regional phases from NORESS, ARCESS and FINESA. The location of the three arrays is shown on the map.
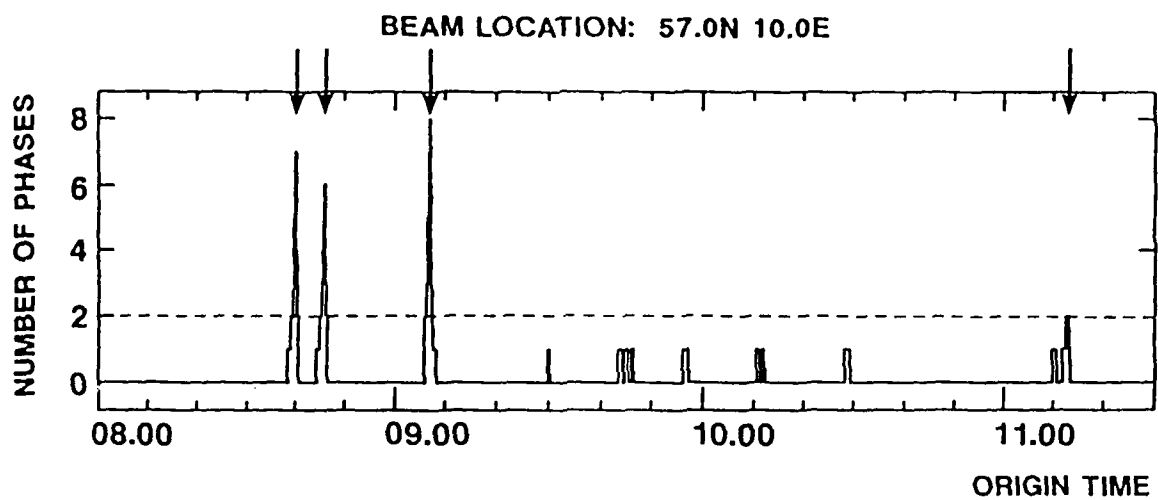
BEAM LOCATION: 57.0N 10.0E

Fig. 2.4.2. Example of typical output trace for one network beam (steered to 57°N, 10°E). In the 3 1/2 hour interval shown, there were 4 confirmed seismic events located in the beam region. These were all correctly detected (arrows), and no false phase associations occurred during the interval.
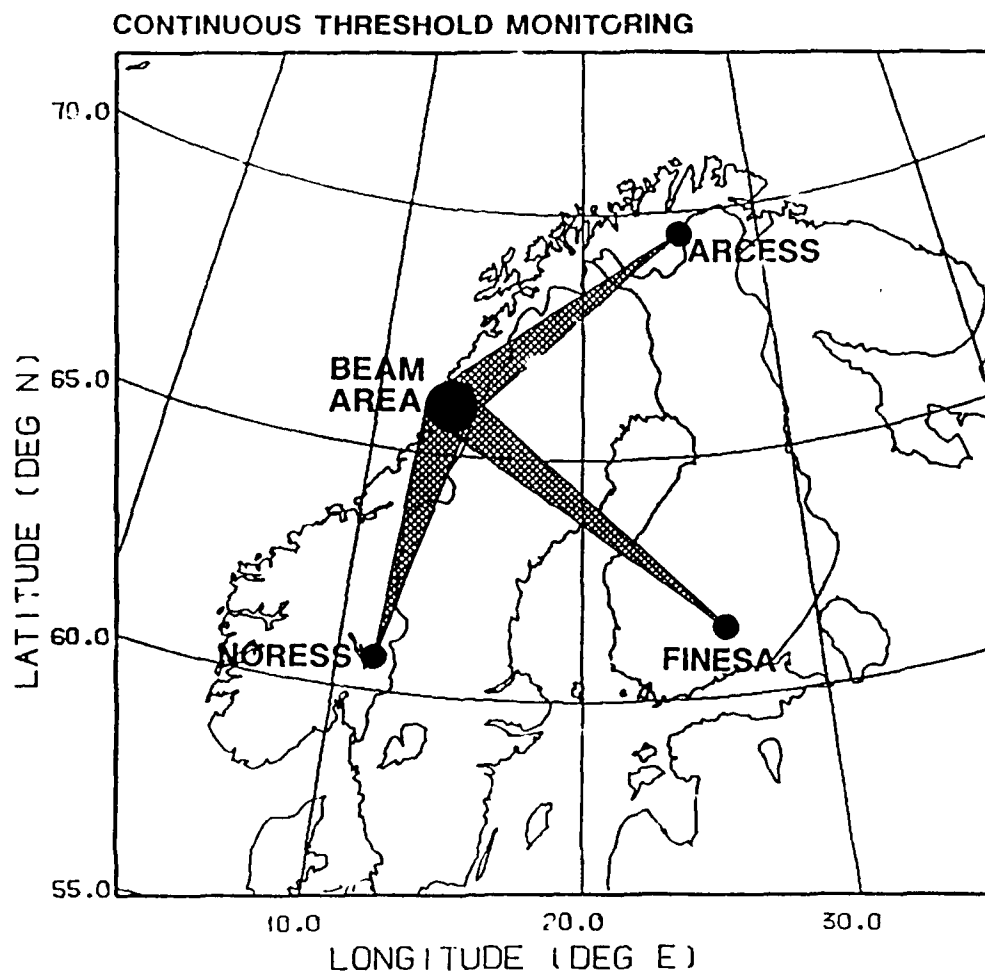
47

CONTINUOUS THRESHOLD MONITORING

Fig. 2.4.3. Location of the beam area used in the example of continuous monitoring of upper magnitude limits on non-detected events. The area covers a circle of approximately 50 km radius, and is situated at similar distances from the three arrays.

48

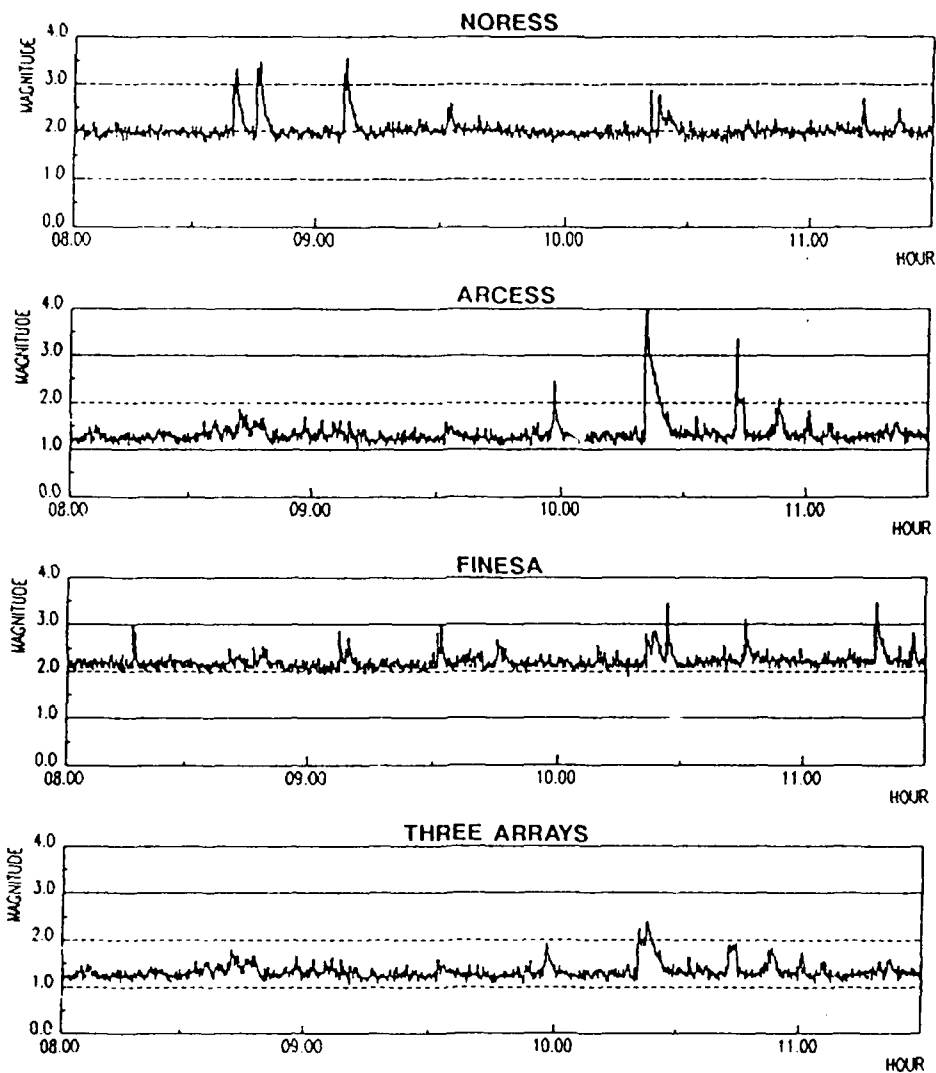**CONTINUOUS THRESHOLD MONITORING - PN PHASE**

90% PROBABILITY

Fig. 2.4.4. Results from the continuous threshold monitoring of the area shown in Fig. 2.4.3 for a 3 1/2 hour period, using Pn phases only. The top three traces show, for each array, the largest magnitude of a possible non-detected event (confidence 90 per cent) as a function of time. The bottom trace shows the result of combining the observations from all three arrays (Pn phase only) as described in the text.

49

CONTINUOUS THRESHOLD MONITORING - PN AND LG PHASES
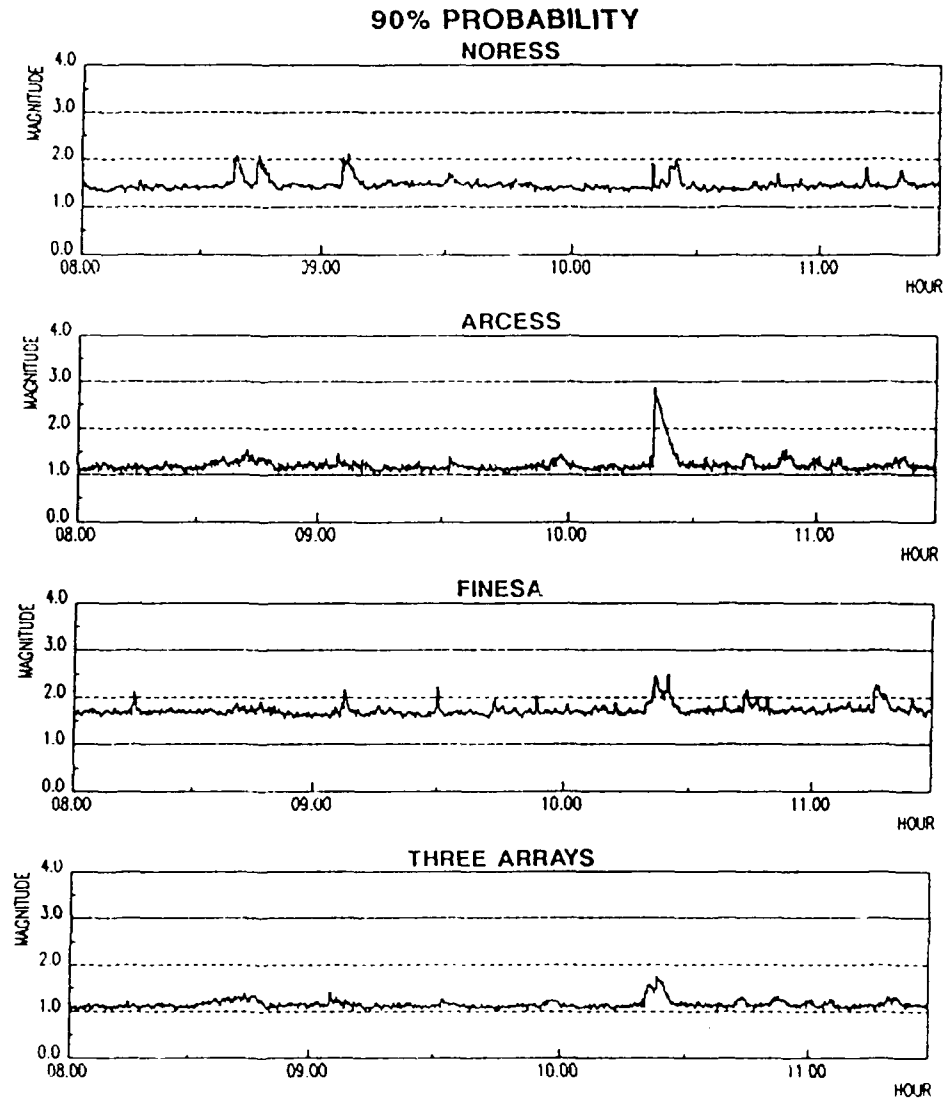
90% PROBABILITY

Fig. 2.4.5. Same as Fig. 2.4.4, but using both the Pn and Lg phases for the upper magnitude limit calculations. Comparing with Fig. 2.4.4, we note that this serves to lower the thresholds, both for each individual array (top three traces) and for the combined results (bottom trace).

50

2.5 Region-specific knowledge derived from analysis of NORESS data

Introduction

The Intelligent Monitoring System (IMS) that is currently being installed at NORSAR, provides functions that allow specific region-dependent knowledge to be taken into account in the automatic processing of multi-array data. To provide such knowledge for enhancement of the performance of IMS is and will remain an important aspect of the research at NORSAR under this contract. In this contribution, we describe two projects that are aimed at deriving region specific knowledge for the benefit of IMS.

Statistics on regional phase attributes from NORESS detection lists

The NORESS detection lists for the period 1985 to 1988 contain more than 200,000 entries, comprising teleseismic, regional and local phase arrivals. The network bulletins for this four-year period published by the University of Bergen, Norway, and the University of Helsinki, Finland, contain altogether 16,000 events that are local or regional to the NORESS array. For each of these 16,000 events, we calculated the expected arrival times at NORESS for the regional phases Pn, Pg, Sn and Lg and then searched the detection lists to see whether the theoretical arrival times matched those of actual phase arrivals detected on the NORESS array. Certain criteria were established in this regard, and, e.g., for the Pn phase these were that the arrival times should not deviate by more than 6 seconds from the predicted ones, the phase velocity (routinely determined by frequency-wavenumber (f-k) analysis for each detected signal) should be within the interval 6-15 km/s, and the arrival azimuths (also determined by f-k analysis) should be within 30° of the predicted values.

This process of merging of the network bulletins with the NORESS detection lists produces a wealth of information on attributes like phase velocities, arrival time residuals and arrival azimuth residuals relative to the network locations. The results may also be used as a basis for compiling data bases of interesting events from specific source regions.

As a result of this merging process, approximately 9,000 arrivals detected on the NORESS array could be classified as either Pn, Pg, Sn or Lg originating from these 16,000 events. Figure 2.5.1 (top) shows the number of Pn phases detected at NORESS from these events and how the corresponding events are distributed on a grid of 1°× 2° blocks (north-south and east-west, respectively). The region around Bergen on the western coast of Norway, the Estonia-Leningrad region of the western USSR, the Finland-USSR border region at around 30°E, 65°N, an area in northern Sweden, and the Kola Peninsula of the USSR stand out clearly in this map. The pattern observed partly reflects the station distribution of the

reporting agencies, but more basically gives an overview of the main mining areas in the Nordic countries and the northwestern USSR. Figure 2.5.1 (bottom) also shows the average phase velocity for Pn phases from events within each block. We see that these velocities fall within the expected range around 8 km/s for most regions of this map. An exception is the Estonia-Leningrad area of the western USSR, where Pn phase velocities averaging more than 10 km/s are observed. Arrival azimuth residuals for the Pn phases are shown in Figure 2.5.2. It is seen that the high Pn phase velocities observed for the Estonia-Leningrad region are accompanied by a rather complex pattern of azimuth residuals.

The azimuth residuals for the Lg phase are shown in Figure 2.5.3. It is noteworthy that the Estonia-Leningrad region exhibits rather moderate Lg azimuth residuals.

It should be noted that phase velocities and arrival azimuths for this study were derived using the conventional or narrow-band f-k analysis method. Since 1989, the broad-band f-k method is used in the analysis of all array data at NORSAR, and will also be used by the IMS. Several studies have testified that the broad-band approach is more stable than the narrow-band method, so a new investigation along the lines of this study should be undertaken, based on the detection lists for 1989.

A detailed study of 103 events in the western Norway area

Another investigation aimed at deriving region-specific knowledge from analysis of NORESS data was a detailed study of 103 events in the western Norway area. The locations of these events are shown in Figure 2.5.4. The large majority of the events are in the distance interval 250-700 km and azimuth interval 210°-330°, relative to NORESS. All phases that could be picked for each of the 103 events were subjected to f-k analysis, using both the narrow-band and broad-band estimation method. The arrival azimuths derived from these analyses were compared with arrival azimuths calculated from the network locations published by the University of Bergen, Norway, and the British Geological Survey.

Arrival azimuth residuals (defined as azimuth estimated from f-k analysis minus azimuth according to the network bulletin) for these events for the Pn, Pg, Sn and Lg phases are plotted as function of network azimuths in Figure 2.5.5 for the broad-band estimation method, and in Figure 2.5.6 for the narrow-band estimation method. It is clearly seen that the broad-band method provides the more stable estimates, and the standard deviation of the azimuth residuals for the broad-band method were found to be of the order of 5-7 degrees, as opposed to 7-11 degrees for the narrow-band method. The smallest standard deviations were found for the crustal phases Pg and Lg.

An interesting observation is that for the Pn and Sn phases, the azimuths (estimated by the broad-band method) deviate systematically from the 'true'

values, in the sense that the residuals are negative for azimuths in the range 210°-270° and positive for azimuths between 270° and 320°. These results indicate that laterally varying structures near the crust-mantle boundary rather than structure within the crust are important in the sense that they influence the azimuths estimated at NORESS. More work is needed in order to gain further insight and understanding of these effects.

Conclusions

The merging of the complete NORESS detection lists for the period 1985-1988 with the regional network bulletins results in a large amount of statistical information on characteristics of regional phases in Fennoscandia and adjacent areas. Similar information will result from merging with the ARCESS and FINESA detection lists. The knowledge gained from this exercise will be of relevance and importance to the IMS, and it is anticipated that this knowledge will be represented in IMS's knowledge base.

A special study of 103 events recorded at NORESS from the western Norway area is another example of what kind of studies that must be undertaken in order to obtain region-specific knowledge needed by the IMS. Among other results, this special study established that the arrival azimuth residuals observed at NORESS for the Pn and Sn phases vary rather systematically with source region in the western Norway area.

S. Mykkeltveit
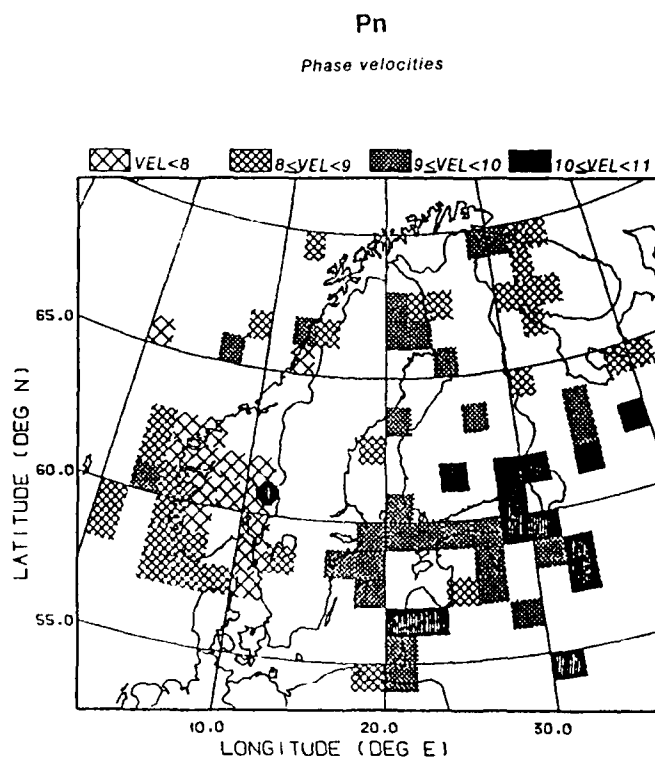S. Kibsgaard, Univ. of Oslo
T. Kværna

Pn

Number of detections
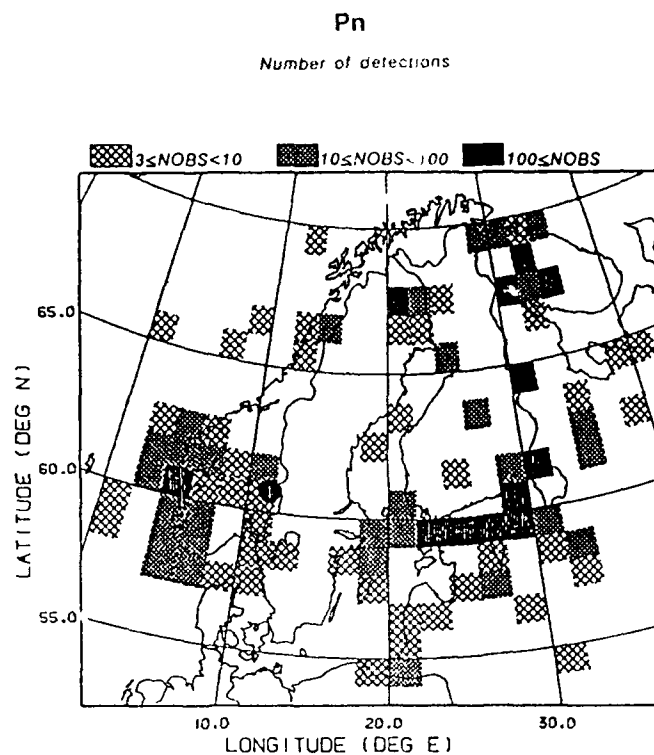

Pn

Phase velocities

Fig. 2.5.1. *Top:* Number of Pn phases (NOBS) detected at NORESS from the various source areas. *Bottom:* Corresponding average Pn velocities (VEL). The location of NORESS is indicated by a special symbol.
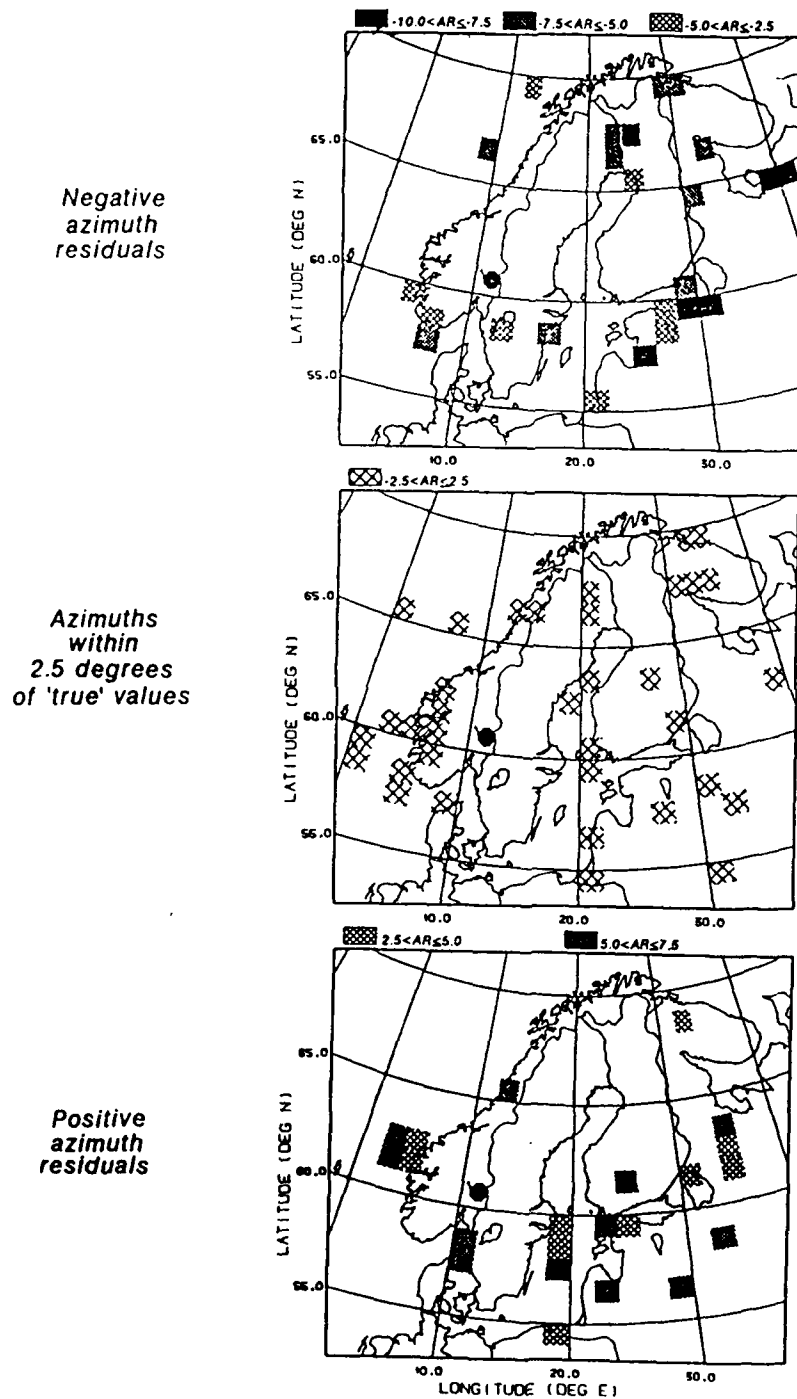
Pn

Fig. 2.5.2. Azimuth residuals (AR = estimated azimuth minus 'true' azimuth, in degrees) for Pn phases detected at NORESS.

Lg

Negative azimuth residuals

Azimuths within 2.5 degrees of 'true' values

Positive azimuth residuals

Fig. 2.5.3. Same as Fig. 2.5.2, but for the Lg phase.
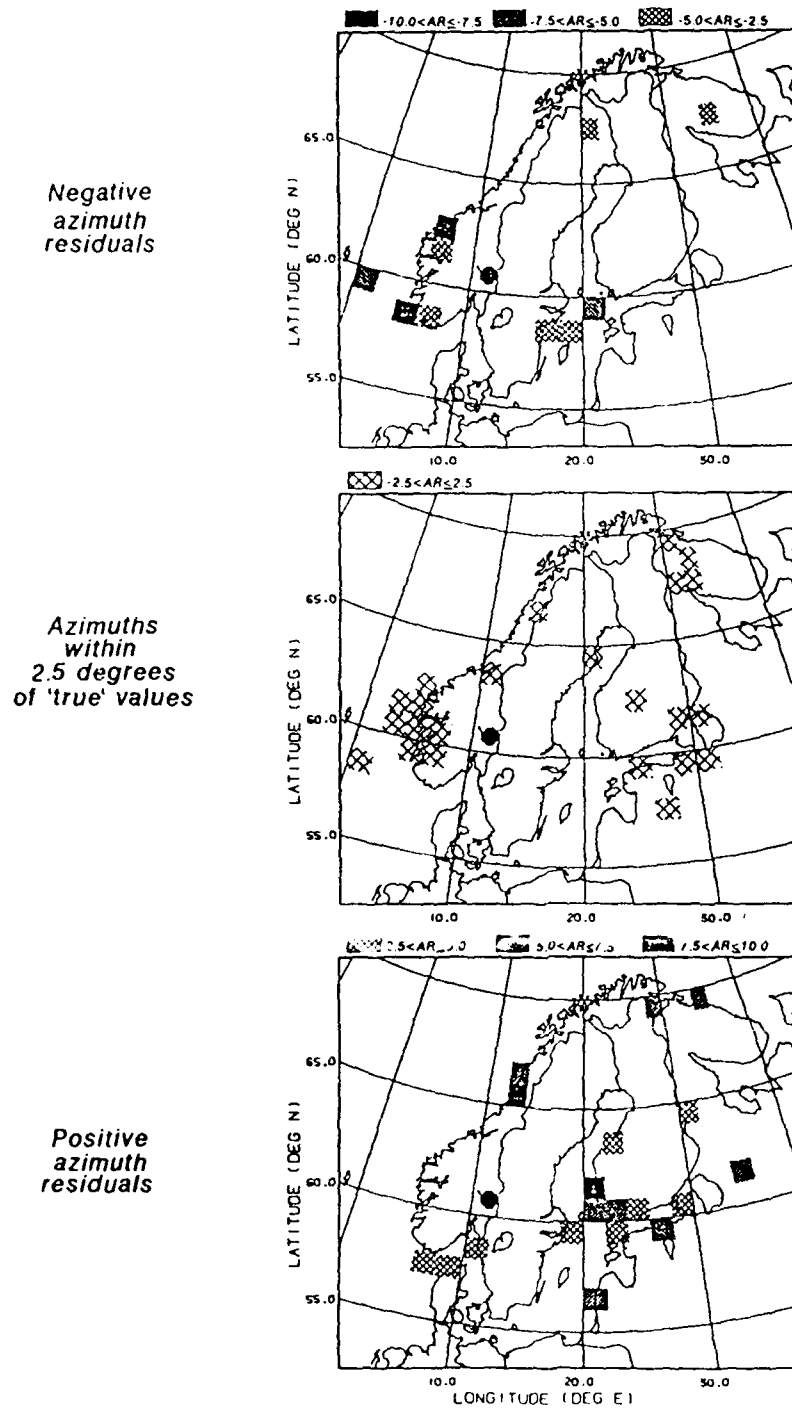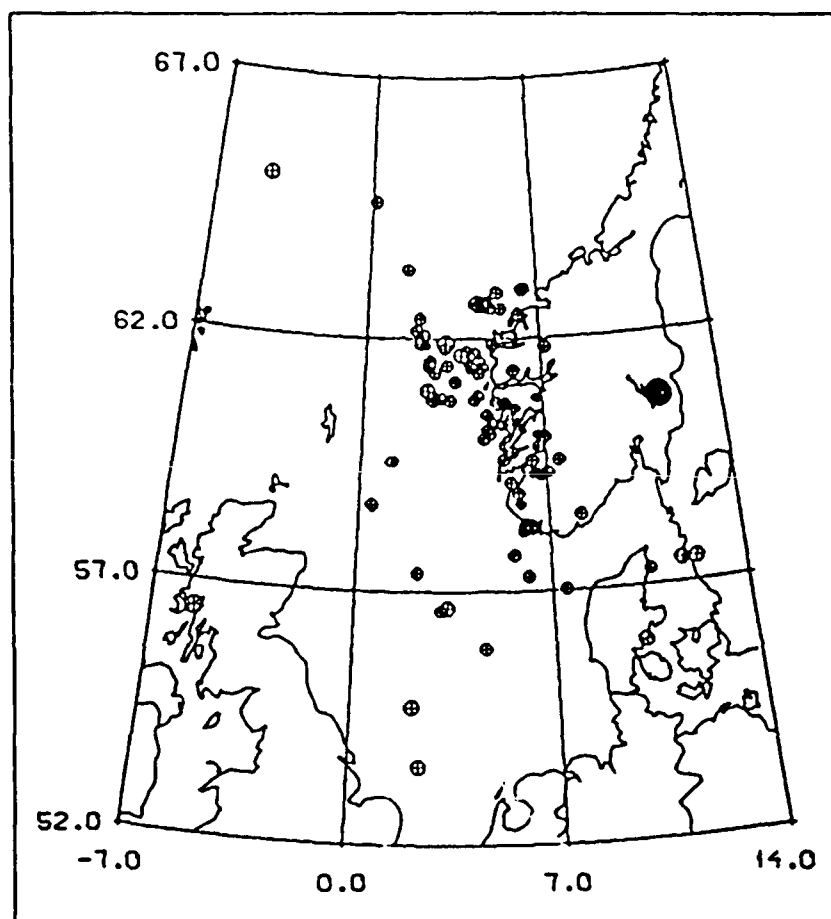
Fig. 2.5.4. The map shows the location of the 103 events in the western Norway region used in this study. The location of NORESS is indicated by a special symbol.
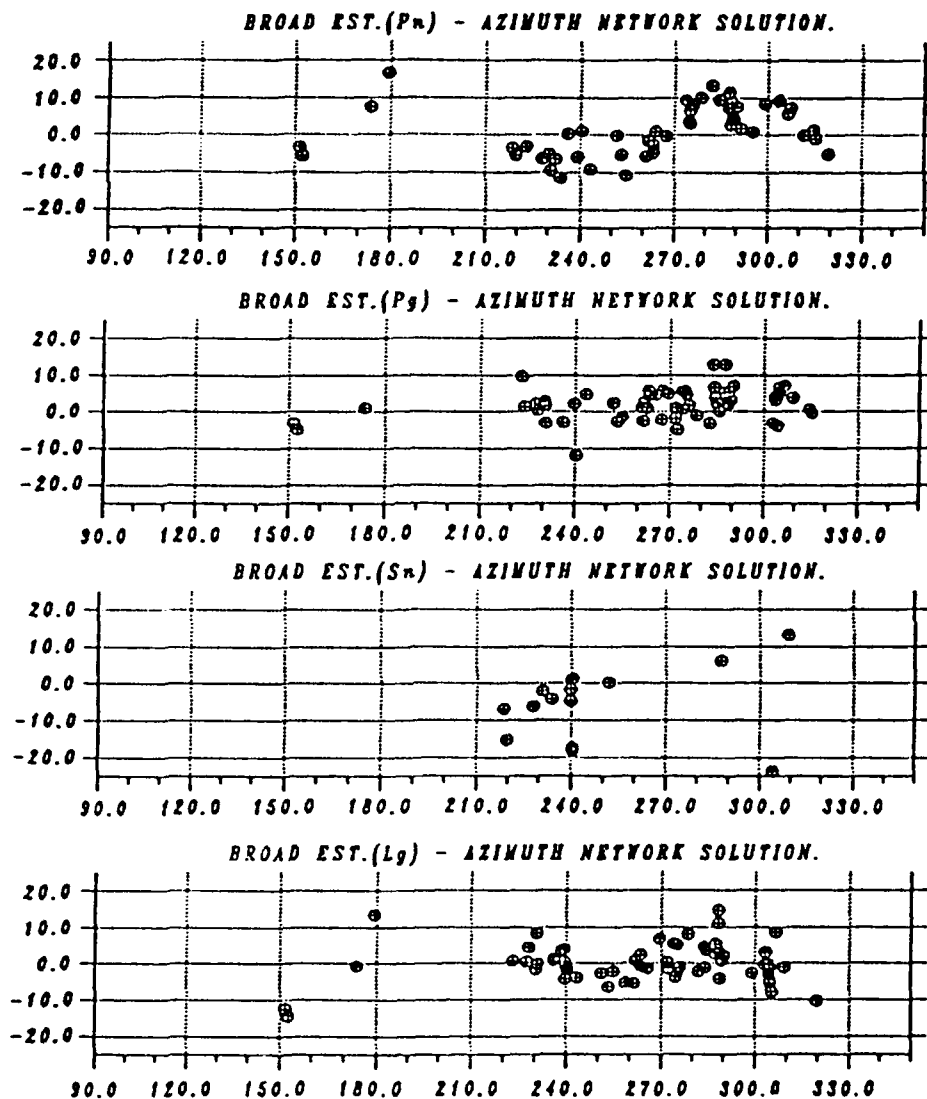
Fig. 2.5.5. The figure shows the azimuth residuals as function of 'true' azimuths, for the broad-band estimation method. The residuals are given (from top to bottom) for the Pn, Pg, Sn and Lg phases.

NBFK EST.(Pn) - AZIMUTH NETW. SOLUTION.

NBFK EST.(Pg) - AZIMUTH NETW. SOLUTION.

NBFK EST.(Sn) - AZIMUTH NETW. SOLUTION.
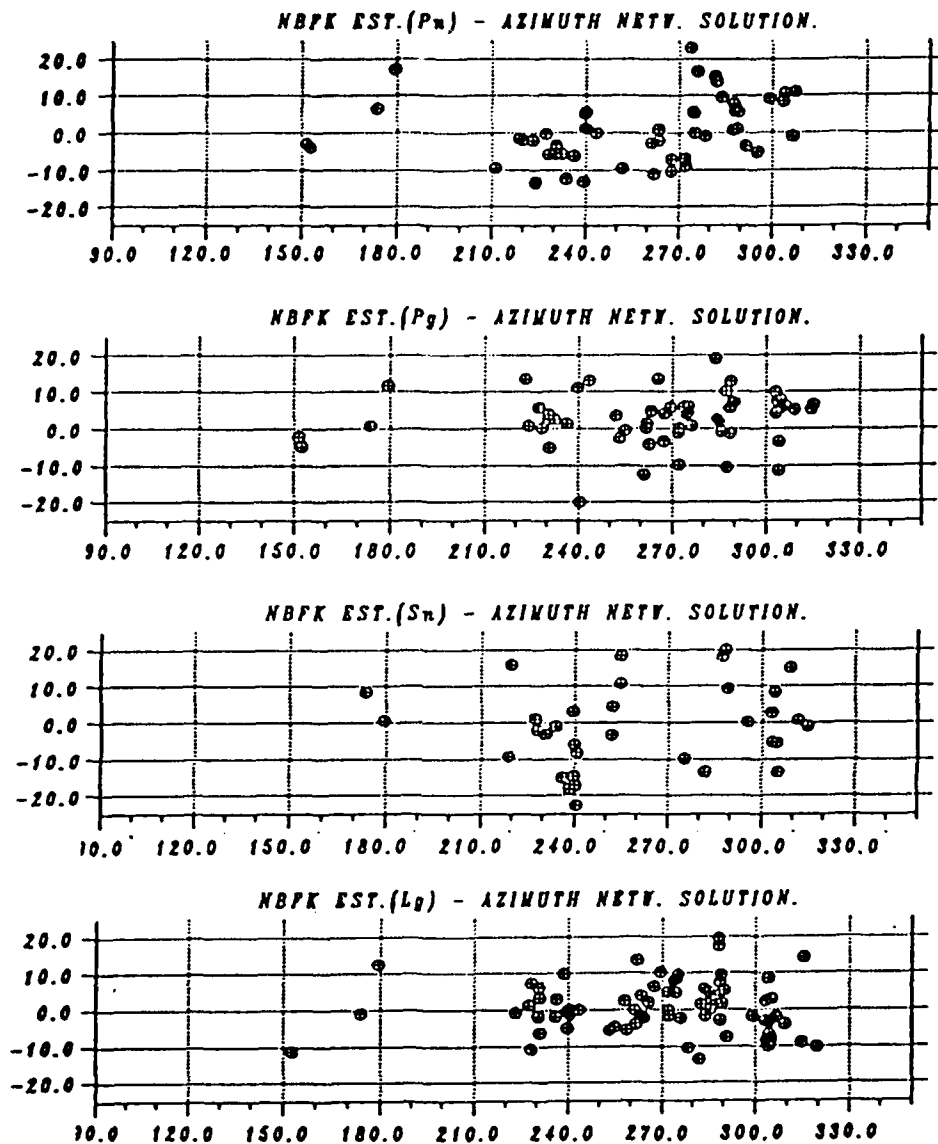
NBFK EST.(Lg) - AZIMUTH NETW. SOLUTION.

Fig. 2.5.6. Same as Fig. 2.5.5, but for the narrow- band estimation method.

Prof. Thomas Ahrens
Seismological Lab, 252-21
Division of Geological & Planetary Sciences
California Institute of Technology
Pasadena, CA 91125

Prof. Charles B. Archambeau
CIRES
University of Colorado
Boulder, CO 80309

Prof. Muawia Barazangi
Institute for the Study of the Continent
Cornell University
Ithaca, NY 14853

Dr. Douglas R. Baumgardt
ENSCO, Inc
5400 Port Royal Road
Springfield, VA 22151-2388

Prof. Jonathan Berger
IGPP, A-025
Scripps Institution of Oceanography
University of California, San Diego
La Jolla, CA 92093

Dr. Lawrence J. Burdick
Woodward-Clyde Consultants
566 El Dorado Street
Pasadena, CA 91109-3245

Dr. Karl Coyner
New England Research, Inc.
76 Olcott Drive
White River Junction, VT 05001

Prof. Vernon F. Cormier
Department of Geology & Geophysics
U-45, Room 207
The University of Connecticut
Storrs, CT 06268

Prof. Steven Day
Department of Geological Sciences
San Diego State University
San Diego, CA 92182

Dr. Zoltan A. Der
ENSCO, Inc.
5400 Port Royal Road
Springfield, VA 22151-2388

Prof. John Ferguson
Center for Lithospheric Studies
The University of Texas at Dallas
P.O. Box 830688
Richardson, TX 75083-0688

Prof. Stanley Flatte
Applied Sciences Building
University of California
Santa Cruz, CA 95064

Dr. Alexander Florence
SRI International
333 Ravenswood Avenue
Menlo Park, CA 94025-3493

Prof. Henry L. Gray
Vice Provost and Dean
Department of Statistical Sciences
Southern Methodist University
Dallas, TX 75275

Dr. Indra Gupta
Teledyne Geotech
314 Montgomery Street
Alexandria, VA 22314

Prof. David G. Harkrider
Seismological Laboratory
Division of Geological & Planetary Sciences
California Institute of Technology
Pasadena, CA 91125

Prof. Donald V. Helmberger
Seismological Laboratory
Division of Geological & Planetary Sciences
California Institute of Technology
Pasadena, CA 91125

Prof. Eugene Herrin
Institute for the Study of Earth and Man
GeophysicalLaboratory
Southern Methodist University
Dallas, TX 75275

Prof. Robert B. Herrmann
Department of Earth & Atmospheric Sciences
St. Louis University
St. Louis, MO 63156

Prof. Bryan Isacks
Cornell University
Department of Geological Sciences
SNEE Hall
Ithaca, NY 14850

Dr. Rong-Song Jih
Teledyne Geotech
314 Montgomery Street
Alexandria, VA 22314

Dr. Gary McCartor
Mission Research Corporation
735 State Street
P.O. Drawer 719
Santa Barbara, CA 93102 (2 copies)

Prof. Lane R. Johnson
Seismographic Station
University of California
Berkeley, CA 94720

Prof. Thomas V. McEvilly
Seismographic Station
University of California
Berkeley, CA 94720

Prof. Alan Kafka
Department of Geology & Geophysics
Boston College
Chestnut Hill, MA 02167

Dr. Keith L. McLaughlin
S-CUBED
A Division of Maxwell Laboratory
P.O. Box 1620
La Jolla, CA 92038-1620

Prof. Fred K. Lamb
University of Illinois at Urbana-Champaign
Department of Physics
1110 West Green Street
Urbana, IL 61801

Prof. William Menke
Lamont-Doherty Geological Observatory
of Columbia University
Palisades, NY 10964

Prof. Charles A. Langston
Geosciences Department
403 Deike Building
The Pennsylvania State University
University Park, PA 16802

Stephen Miller
SRI International
333 Ravenswood Avenue
Box AF 116
Menlo Park, CA 94025-3493

Prof. Thorne Lay
Department of Geological Sciences
1006 C.C. Little Building
University of Michigan
Ann Arbor, MI 48109-1063

Prof. Bernard Minster
IGPP, A-025
Scripps Institute of Oceanography
University of California, San Diego
La Jolla, CA 92093

Prof. Arthur Lerner-Lam
Lamont-Doherty Geological Observatory
of Columbia University
Palisades, NY 10964

Prof. Brian J. Mitchell
Department of Earth & Atmospheric Sciences
St. Louis University
St. Louis, MO 63156

Dr. Christopher Lynnes
Teledyne Geotech
314 Montgomery Street
Alexandria, VA 22314

Mr. Jack Murphy
S-CUBED, A Division of Maxwell Laboratory
11800 Sunrise Valley Drive
Suite 1212
Reston, VA 22091 (2 copies)

Prof. Peter Malin
University of California at Santa Barbara
Institute for Crustal Studies
Santa Barbara, CA 93106

Dr. Bao Nguyen
GL/LWH
Hanscom AFB, MA 01731-5000

Dr. Randolph Martin, III
New England Research, Inc.
76 Olcott Drive
White River Junction, VT 05001

Prof. John A. Orcutt
IGPP, A-025
Scripps Institute of Oceanography
University of California, San Diego
La Jolla, CA 92093

Prof. Keith Priestley
University of Nevada
Mackay School of Mines
Reno, NV 89557

Prof. Clifford Thurber
University of Wisconsin-Madison
Department of Geology & Geophysics
1215 West Dayton Street
Madison, WS 53706

Prof. Paul G. Richards
Lamont-Doherty Geological Observatory
of Columbia University
Palisades, NY 10964

Prof. M. Nafi Toksoz
Earth Resources Lab
Massachusetts Institute of Technology
42 Carleton Street
Cambridge, MA 02142

Dr. Wilmer Rivers
Teledyne Geotech
314 Montgomery Street
Alexandria, VA 22314

Prof. John E. Vidale
University of California at Santa Cruz
Seismological Laboratory
Santa Cruz, CA 95064

Dr. Alan S. Ryall, Jr.
Center for Seismic Studies
1300 North 17th Street
Suite 1450
Arlington, VA 22209-2308

Prof. Terry C. Wallace
Department of Geosciences
Building #77
University of Arizona
Tucson, AZ 85721

Prof. Charles G. Sammis
Center for Earth Sciences
University of Southern California
University Park
Los Angeles, CA 90089-0741

Dr. Raymond Willeman
GL/LWH
Hanscom AFB, MA 01731-5000

Prof. Christopher H. Scholz
Lamont-Doherty Geological Observatory
of Columbia University
Palisades, NY 10964

Dr. Lorraine Wolf
GL/LWH
Hanscom AFB, MA 01731-5000

Prof. David G. Simpson
Lamont-Doherty Geological Observatory
of Columbia University
Palisades, NY 10964

Prof. Francis T. Wu
Department of Geological Sciences
State University of New York
at Binghamton
Vestal, NY 13901

Dr. Jeffrey Stevens
S-CUBED
A Division of Maxwell Laboratory
P.O. Box 1620
La Jolla, CA 92038-1620

Prof. Brian Stump
Institute for the Study of Earth & Man
Geophysical Laboratory
Southern Methodist University
Dallas, TX 75275

Prof. Jeremiah Sullivan
University of Illinois at Urbana-Champaign
Department of Physics
1110 West Green Street
Urbana, IL 61801

Dr. Monem Abdel-Gawad
Rockwell International Science Center
1049 Camino Dos Rios
Thousand Oaks, CA 91360

Prof. Keiiti Aki
Center for Earth Sciences
University of Southern California
University Park
Los Angeles, CA 90089-0741

Prof. Shelton S. Alexander
Geosciences Department
403 Deike Building
The Pennsylvania State University
University Park, PA 16802

Dr. Ralph Archuleta
Department of Geological Sciences
University of California at Santa Barbara
Santa Barbara, CA 93102

Dr. Thomas C. Bache, Jr.
Science Applications Int'l Corp.
10210 Campus Point Drive
San Diego, CA 92121 (2 copies)

J. Barker
Department of Geological Sciences
State University of New York
at Binghamton
Vestal, NY 13901

Dr. T.J. Bennett
S-CUBED
A Division of Maxwell Laboratory
11800 Sunrise Valley Drive, Suite 1212
Reston, VA 22091

Mr. William J. Best
907 Westwood Drive
Vienna, VA 22180

Dr. N. Biswas
Geophysical Institute
University of Alaska
Fairbanks, AK 99701

Dr. G.A. Bollinger
Department of Geological Sciences
Virginia Polytechnical Institute
21044 Derring Hall
Blacksburg, VA 24061

Dr. Stephen Bratt
Science Applications Int'l Corp.
10210 Campus Point Drive
San Diego, CA 92121

Michael Browne
Teledyne Geotech
3401 Shiloh Road
Garland, TX 75041

Mr. Roy Burger
1221 Serry Road
Schenectady, NY 12309

Dr. Robert Burridge
Schlumberger-Doll Research Center
Old Quarry Road
Ridgefield, CT 06877

Dr. Jerry Carter
Rondout Associates
P.O. Box 224
Stone Ridge, NY 12484

Dr. W. Winston Chan
Teledyne Geotech
314 Montgomery Street
Alexandria, VA 22314-1581

Dr. Theodore Cherry
Science Horizons, Inc.
710 Encinitas Blvd., Suite 200
Encinitas, CA 92024 (2 copies)

Prof. Jon F. Claerbout
Department of Geophysics
Stanford University
Stanford, CA 94305

Prof. Robert W. Clayton
Seismological Laboratory
Division of Geological & Planetary Sciences
California Institute of Technology
Pasadena, CA 91125

Prof. F. A. Dahlen
Geological and Geophysical Sciences
Princeton University
Princeton, NJ 08544-0636

Prof. Anton W. Dainty
Earth Resources Lab
Massachusetts Institute of Technology
42 Carleton Street
Cambridge, MA 02142

Prof. Adam Dziewonski
Hoffman Laboratory
Harvard University
20 Oxford St
Cambridge, MA 02138

Prof. John Ebel
Department of Geology & Geophysics
Boston College
Chestnut Hill, MA 02167

Eric Fielding
SNEE Hall
INSTOC
Cornell University
Ithaca, NY 14853

Prof. Donald Forsyth
Department of Geological Sciences
Brown University
Providence, RI 02912

Prof. Art Frankel
Mail Stop 922
Geological Survey
790 National Center
Reston, VA 22092

Dr. Anthony Gangi
Texas A&M University
Department of Geophysics
College Station, TX 77843

Dr. Freeman Gilbert
Inst. of Geophysics & Planetary Physics
University of California, San Diego
P.O. Box 109
La Jolla, CA 92037

Mr. Edward Giller
Pacific Sierra Research Corp.
1401 Wilson Boulevard
Arlington, VA 22209

Dr. Jeffrey W. Given
Sierra Geophysics
11255 Kirkland Way
Kirkland, WA 98033

Prof. Stephen Grand
University of Texas at Austin
Department of Geological Sciences
Austin, TX 78713-7909

Prof. Roy Greenfield
Geosciences Department
403 Deike Building
The Pennsylvania State University
University Park, PA 16802

Dan N. Hagedorn
Battelle
Pacific Northwest Laboratories
Battelle Boulevard
Richland, WA 99352

Kevin Hutchenson
Department of Earth Sciences
St. Louis University
3507 Laclede
St. Louis, MO 63103

Prof. Thomas H. Jordan
Department of Earth, Atmospheric
  and Planetary Sciences
Massachusetts Institute of Technology
Cambridge, MA 02139

Robert C. Kemerait
ENSCO, Inc.
445 Pineda Court
Melbourne, FL 32940

William Kikendall
Teledyne Geotech
3401 Shiloh Road
Garland, TX 75041

Prof. Leon Knopoff
University of California
Institute of Geophysics & Planetary Physics
Los Angeles, CA 90024

Prof. L. Timothy Long
School of Geophysical Sciences
Georgia Institute of Technology
Atlanta, GA 30332

Prof. Art McGarr
Mail Stop 977
Geological Survey
345 Middlefield Rd.
Menlo Park, CA 94025

-5-

Dr. George Mellman
Sierra Geophysics
11255 Kirkland Way
Kirkland, WA 98033

Dr. Richard Sailor
TASC Inc.
55 Walkers Brook Drive
Reading, MA 01867

Prof. John Nabelek
College of Oceanography
Oregon State University
Corvallis, OR 97331

Thomas J. Sereno, Jr.
Science Application Int'l Corp.
10210 Campus Point Drive
San Diego, CA 92121

Prof. Geza Nagy
University of California, San Diego
Department of Ames, M.S. B-010
La Jolla, CA 92093

John Sherwin
Teledyne Geotech
3401 Shiloh Road
Garland, TX 75041

Prof. Amos Nur
Department of Geophysics
Stanford University
Stanford, CA 94305

Prof. Robert Smith
Department of Geophysics
University of Utah
1400 East 2nd South
Salt Lake City, UT 84112

Prof. Jack Oliver
Department of Geology
Cornell University
Ithaca, NY 14850

Prof. S. W. Smith
Geophysics Program
University of Washington
Seattle, WA 98195

Prof. Robert Phinney
Geological & Geophysical Sciences
Princeton University
Princeton, NJ 08544-0636

Dr. Stewart Smith
IRIS Inc.
1616 North Fort Myer Drive
Suite 1440
Arlington, VA 22209

Dr. Paul Pomeroy
Rondout Associates
P.O. Box 224
Stone Ridge, NY 12484

Dr. George Sutton
Rondout Associates
P.O. Box 224
Stone Ridge, NY 12484

Dr. Jay Pulli
RADIX System, Inc.
2 Taft Court, Suite 203
Rockville, MD 20850

Prof. L. Sykes
Lamont-Doherty Geological Observatory
of Columbia University
Palisades, NY 10964

Dr. Norton Rimer
S-CUBED
A Division of Maxwell Laboratory
P.O. Box 1620
La Jolla, CA 92038-1620

Prof. Pradeep Talwani
Department of Geological Sciences
University of South Carolina
Columbia, SC 29208

Prof. Larry J. Ruff
Department of Geological Sciences
1006 C.C. Little Building
University of Michigan
Ann Arbor, MI 48109-1063

Prof. Ta-liang Teng
Center for Earth Sciences
University of Southern California
University Park
Los Angeles, CA 90089-0741

Dr. R.B. Tittmann
Rockwell International Science Center
1049 Camino Dos Rios
P.O. Box 1085
Thousand Oaks, CA 91360

Dr. Gregory van der Vink
IRIS, Inc.
1616 North Fort Myer Drive
Suite 1440
Arlington, VA 22209

William R. Walter
Seismological Laboratory
University of Nevada
Reno, NV 89557

Dr. Gregory Wojcik
Weidlinger Associates
4410 El Camino Real
Suite 110
Los Altos, CA 94022

Prof. John H. Woodhouse
Hoffman Laboratory
Harvard University
20 Oxford Street
Cambridge, MA 02138

Dr. Gregory B. Young
ENSCO, Inc.
5400 Port Royal Road
Springfield, VA 22151-2388

Dr. Ralph Alewine III
DARPA/NMRO
1400 Wilson Boulevard
Arlington, VA 01731-5000

Paul Johnson
ESS-4, Mail Stop J979
Los Alamos National Laboratory
Los Alamos, NM 87545

Mr. James C. Battis
GL/LWH
Hanscom AFB, MA 22209-2308

Janet Johnston
GL/LWH
Hanscom AFB, MA 01731-5000

Dr. Robert Blandford
DARPA/NMRO
1400 Wilson Boulevard
Arlington, VA 87185

Dr. Katharine Kadinsky-Cade
GL/LWH
Hanscom AFB, MA 01731-5000

Eric Chael
Division 9241
Sandia Laboratory
Albuquerque, NM 01731-5000

Ms. Ann Kerr
IGPP, A-025
Scripps Institute of Oceanography
University of California, San Diego
La Jolla, CA 92093

Dr. John J. Cipar
GL/LWH
Hanscom AFB, MA 01731-5000

Dr. Max Koontz
US Dept of Energy/DP 5
Forrestal Building
1000 Independence Avenue
Washington, DC 20585

Mr. Jeff Duncan
Office of Congressman Markey
2133 Rayburn House Bldg.
Washington, D.C. 20515

Dr. W.H.K. Lee
Office of Earthquakes, Volcanoes,
& Engineering
345 Middlefield Road
Menlo Park, CA 94025

Dr. Jack Evernden
USGS - Earthquake Studie
345 Middlefield Road
Menlo Park, CA 94025

Dr. William Leith
U.S. Geological Survey
Mail Stop 928
Reston, VA 22092

Art Frankel
USGS
922 National Center
Reston, VA 22092

Dr. Richard Lewis
Director, Earthquake Engineering & Geophysics
U.S. Army Corps of Engineers
Box 631
Vicksburg, MS 39180

Dr. T. Hanks
USGS
Nat'l Earthquake Research Center
345 Middlefield Road
Menlo Park, CA 94025

James F. Lewkowicz
GL/LWH
Hanscom AFB, MA 01731-5000

Dr. James Hannon
Lawrence Livermore Nat'l Laboratory
P.O. Box 808
Livermore, CA 94550

Mr. Alfred Lieberman
ACDA/VI-OA'State Department Bldg
Room 5726
320 - 21st Street, NW
Washington, DC 20451

Stephen Mangino
GL/LWH
Hanscom AFB, MA 01731-5000

Dr. Frank F. Pilotte
HQ AFTAC/TT
Patrick AFB, FL 32925-6001

Dr. Robert Masse
Box 25046, Mail Stop 967
Denver Federal Center
Denver, CO 80225

Katie Poley
CIA-OSWR/NED
Washington, DC 20505

Art McGarr
U.S. Geological Survey, MS-977
345 Middlefield Road
Menlo Park, CA 94025

Mr. Jack Rachlin
U.S. Geological Survey
Geology, Rm 3 C136
Mail Stop 928 National Center
Reston, VA 22092

Richard Morrow
ACDA/VI, Room 5741
320 21st Street N.W
Washington, DC 20451

Dr. Robert Reinke
WL/NTESG
Kirtland AFB, NM 87117-6008

Dr. Keith K. Nakanishi
Lawrence Livermore National Laboratory
P.O. Box 808, L-205
Livermore, CA 94550

Dr. Byron Ristvet
HQ DNA, Nevada Operations Office
Attn: NVCG
P.O. Box 98539
Las Vegas, NV 89193

Dr. Carl Newton
Los Alamos National Laboratory
P.O. Box 1663
Mail Stop C335, Group ESS-3
Los Alamos, NM 545

Dr. George Rothe
HQ AFTAC/TGR
Patrick AFB, FL 32925-6001

Dr. Kenneth H. Olsen
Los Alamos Scientific Laboratory
P.O. Box 1663
Mail Stop C335, Group ESS-3
Los Alamos, NM 87545

Dr. Michael Shore
Defense Nuclear Agency/SPSS
6801 Telegraph Road
Alexandria, VA 22310

Howard J. Patton
Lawrence Livermore National Laboratory
P.O. Box 808, L-205
Livermore, CA 94550

Donald L. Springer
Lawrence Livermore National Laboratory
P.O. Box 808, L-205
Livermore , CA 94550

Mr. Chris Paine
Office of Senator Kennedy, SR 315

United States Senate
Washington, DC 20510

Dr. Lawrence Turnbull
OSWR/NED
Central Intelligence Agency, Room 5G48
Washington, DC 20505

Colonel Jerry J. Perrizo
AFOSR/NP, Building 410
Bolling AFB
Washington, DC 20332-6448

Dr. Thomas Weaver
Los Alamos National Laboratory
P.O. Box 1663, Mail Stop C335
Los Alamos, NM 87545

J.J. Zucca
Lawrence Livermore National Laboratory
Box 808
Livermore, CA 94550

Defense Technical Information Center
Cameron Station
Alexandria, VA 22314 (5 copies)

GL/SULL
Research Library
Hanscom AFB , MA 01731-5000 (2 copies)

Defense Intelligence Agency
Directorate for Scientific &
Technical Intelligence
Washington, DC 20301

Secretary of the Air Force (SAFRD)

Washington, DC 20330

AFTAC/CA
(STINFO)
Patrick AFB, FL 32925-6001

Office of the Secretary Defense
DDR & E
Washington, DC 20330

TACTEC
Battelle Memorial Institute
505 King Avenue
Columbus, OH 43201 (Final Report Only)

HQ DNA
Attn: Technical Library
Washington, DC 20305

Mr. Charles L. Taylor
GL/LWH

Hanscom AFB, MA 01731-5000

DARPA/RMO/RETRIEVAL
1400 Wilson Boulevard
Arlington, VA 22209

DARPA/RMO/Security Office
1400 Wilson Boulevard
Arlington, VA 22209

Geophysics Laboratory
Attn: XO
Hanscom AFB, MA 01731-5000

Geophysics Laboratory
Attn: LW
Hanscom AFB, MA 01731-5000

DARPA/PM
1400 Wilson Boulevard
Arlington, VA 22209

Dr. Ramon Cabre, S.J.
Observatorio San Calixto
Casilla 5939
La Paz, Bolivia

Prof. Hans-Peter Harjes
Institute for Geophysik
Ruhr University/Bochum
P.O. Box 102148
4630 Bochum 1, FRG

Prof. Eystein Husebye
NTNF/NORSAR
P.O. Box 51
N-2007 Kjeller, NORWAY

Prof. Brian L.N. Kennett
Research School of Earth Sciences
Institute of Advanced Studies
G.P.O. Box 4
Canberra 2601, AUSTRALIA

Dr. Bernard Massinon
Societe Radiomana
27 rue Claude Bernard
75005 Paris, FRANCE (2 Copies)

Dr. Pierre Mecheler
Societe Radiomana
27 rue Claude Bernard
75005 Paris, FRANCE

Dr. Svein Mykkeltveit
NTNF/NORSAR
P.O. Box 51
N-2007 Kjeller, NORWAY

Dr. Peter Basham
Earth Physics Branch
Geological Survey of Canada
1 Observatory Crescent
Ottawa, Ontario, CANADA K1A 0Y3

Dr. Eduard Berg
Institute of Geophysics
University of Hawaii
Honolulu, HI 96822

Dr. Michel Bouchon
I.R.I.G.M.-B.P. 68
38402 St. Martin D'Heres
Cedex, FRANCE

Dr. Hilmar Bungum
NTNF/NORSAR
P.O. Box 51
N-2007 Kjeller, NORWAY

Dr. Michel Campillo
Observatoire de Grenoble
I.R.I.G.M.-B.P. 53
38041 Grenoble, FRANCE

Dr. Kin Yip Chun
Geophysics Division
Physics Department
University of Toronto
Ontario, CANADA M5S 1A7

Dr. Alan Douglas
Ministry of Defense
Blacknest, Brimpton
Reading RG7-4RS, UNITED KINGDOM

Dr. Roger Hansen
NTNF/NORSAR
P.O. Box 51
N-2007 Kjeller, NORWAY

Dr. Manfred Henger
Federal Institute for Geosciences & Nat'l Res.
Postfach 510153
D-3000 Hanover 51, FRG

Ms. Eva Johannisson
Senior Research Officer
National Defense Research Inst.
P.O. Box 27322
S-102 54 Stockholm, SWEDEN

Dr. Fekadu Kebede
Seismological Section
Box 12019
S-750 Uppsala, SWEDEN

Dr. Tormod Kvaerna
NTNF/NORSAR
P.O. Box 51
N-2007 Kjeller, NORWAY

Dr. Peter Marshal
Procurement Executive
Ministry of Defense
Blacknest, Brimpton
Reading FG7-4RS, UNITED KINGDOM

Prof. Ari Ben-Menahem
Department of Applied Mathematics
Weizman Institute of Science
Rehovot, ISRAEL 951729

Dr. Robert North
Geophysics Division
Geological Survey of Canada
1 Observatory Crescent
Ottawa, Ontario, CANADA K1A 0Y3

Dr. Frode Ringdal
NTNF/NORSAR
P.O. Box 51
N-2007 Kjeller, NORWAY

Dr. Jorg Schlittenhardt
Federal Institute for Geosciences & Nat'l Res.
Postfach 510153
D-3000 Hannover 51, FEDERAL REPUBLIC OF GERMANY

Prof. Daniel Walker
University of Hawaii
Institute of Geophysics
Honolulu, HI 96822